

PARAMETRIC INVESTIGATION OF HULL SHAPED FUSELAGE
FOR AMPHIBIOUS UAV

A THESIS SUBMITTED TO
THE GRADUATE SCHOOL OF NATURAL AND APPLIED SCIENCES
OF
MIDDLE EAST TECHNICAL UNIVERSITY

BY

EMRE SAZAK

IN PARTIAL FULFILLMENT OF THE REQUIREMENTS
FOR
THE DEGREE OF MASTER OF SCIENCE
IN
AEROSPACE ENGINEERING

JANUARY 2017

Approval of the thesis:

**PARAMETRIC INVESTIGATION OF HULL SHAPED FUSELAGE
FOR AMPHIBIOUS UAV**

submitted by **EMRE SAZAK** in partial fulfillment of the requirements for the degree of **Master of Science in Aerospace Engineering Department, Middle East Technical University** by,

Prof. Dr. Gülbin Dural Ünver
Dean, Graduate School of Natural and Applied Sciences

Prof. Dr. Ozan Tekinalp
Head of Department, Aerospace Engineering

Assoc. Prof. Dr. Dilek Funda Kurtuluş
Supervisor, Aerospace Engineering Dept., METU

Examining Committee Members:

Prof. Dr. Ünver Kaynak
Mechanical Engineering Dept., TOBB ETU

Prof. Dr. Serkan Özgen
Aerospace Engineering Dept., METU

Assoc. Prof. Dr. Dilek Funda Kurtuluş
Aerospace Engineering Dept., METU

Asst. Prof. Dr. Nilay Sezer Uzol
Aerospace Engineering Dept., METU

Asst. Prof. Dr. Kutluk Bilge Arıkan
Mechatronics Engineering Dept., Atılım University

Date: 10.01.2017

I hereby declare that all information in this document has been obtained and presented in accordance with academic rules and ethical conduct. I also declare that, as required by these rules and conduct, I have fully cited and referenced all material and results that are original to this work.

Name, Last name : Emre SAZAK

Signature :

ABSTRACT

PARAMETRIC INVESTIGATION OF HULL SHAPED FUSELAGE FOR AMPHIBIOUS UAV

Sazak, Emre

M.S., Department of Aerospace Engineering

Supervisor: Assoc. Prof. Dr. Dilek Funda Kurtuluş

January 2017, 70 pages

Performance of amphibious unmanned aerial vehicles (UAV's) that take off from and land on water, like seaplanes, greatly depend on hydrodynamic effects as well as aerodynamic effects, therefore their geometries need to be optimized for both. This study mainly investigates the effect of geometric parameters of a generic, hull-shaped fuselage that are constrained by hydrodynamic drivers, such as the step height needed to reduce hydrodynamic drag, sternpost angle and deadrise angle needed for safe landing; on aerodynamic drag of the fuselage under cruise conditions by using the commercial CFD (Computational Fluid Dynamics) code ANSYS Fluent. Study includes a comparison of the experimental results obtained from literature with numerical results around a hull-shaped fuselage at angles of attack varying between -8° to 16° .

Keywords: Amphibious UAV, Computational Fluid Dynamics, Aerodynamics, Hull-Shaped Fuselage.

ÖZ

AMFİBİ İHA İÇİN TEKNE ŞEKLİNDEKİ GÖVDENİN PARAMETRİK İNCELENMESİ

Sazak, Emre

Yüksek Lisans, Havacılık ve Uzay Mühendisliği Bölümü

Tez Yöneticisi: Doç. Dr. Dilek Funda Kurtuluş

Ocak 2017, 70 sayfa

Sudan kalkan ve suya iniş yapan amfibi insansız hava araçlarının (İHA'ların) performansları, deniz uçaklarında olduğu gibi hem aerodinamik hem de hidrodinamik etkilere bağlıdır. Bu sebeple şekilleri her iki etkiye göre de optimize edilmelidir. Bu çalışmada temelde, genel bir tekne biçimli gövdeye ait; hidrodinamik sürüklenmeyi azaltmak için gereken basamak (step) yüksekliği, dümen bodoslama açısı (sternpost angle) ve güvenli iniş için gerekli kalkıntı açısı (deadrise angle) gibi hidrodinamik faktörlerle sınırlanan geometrik parametrelerin seyir halinde aerodinamik sürüklenme kuvvetine olan etkisi, HAD (Hesaplamalı Akışkanlar Dinamiği) programı ANSYS Fluent kullanılarak incelenmektedir. Bu kapsamda ayrıca literatürden elde edilen deneysel sonuçlar ile -8° 'den 16° 'ye kadar değişen hücum açılarında tekne biçimli gövde etrafında elde edilen nümerik sonuçlar karşılaştırılmıştır.

Anahtar Kelimeler: Amfibi İHA, Hesaplamalı Akışkanlar Dinamiği, Aerodinamik, Tekne Şeklinde Gövde.

Dedicated to my family...

ACKNOWLEDGEMENTS

First of all, I would like to thank to my supervisor Assoc. Prof. Dr. Dilek Funda Kurtuluş for her guidance, faith and patience throughout my studies. I have learned a great deal under her tutelage, for which I am deeply grateful.

I am also grateful to my friends Ozan Alican, Semih Özdede, Umut Baykara, Cengiz Özdemir, Berk Gür, Gökay Sedef and Çağrı Gezgüç for their friendship and help throughout my studies.

I would like to thank to my family for encouraging me and believing in me all my life, and for their never-ending support.

Finally, but not least, I would like to thank to my loving wife Duygu, for helping me and enduring with me in overcoming every obstacle along the way. I could not have done it without her.

TABLE OF CONTENTS

ABSTRACT	v
ÖZ.....	vi
ACKNOWLEDGEMENTS	viii
TABLE OF CONTENTS	ix
LIST OF TABLES	xii
LIST OF FIGURES.....	xiv
LIST OF SYMBOLS.....	xvii
LIST OF ABBREVIATIONS	xix
CHAPTER 1 INTRODUCTION.....	1
1.1 Historical Background.....	2
1.2 Literature Survey	4
1.3 Motivation for the Study.....	6
1.4 Purpose of the Study	9
CHAPTER 2 DESIGN PARAMETERS.....	11
2.1 Hull Shape Parameters.....	11
2.1.1 Step.....	14
2.1.2 Deadrise Angle	14
2.1.3 Sternpost Angle	14
2.1.4 Other Parameters	15
2.1.5 Typical Ranges of Design Parameters.....	15
2.2 Analytical Model for Drag Coefficient.....	16
CHAPTER 3 COMPUTATIONAL METHOD	17

3.1	Governing Equations	17
3.2	Turbulence Modelling	18
3.2.1	Spalart-Allmaras.....	19
3.2.2	Standard k- ϵ	19
3.2.3	Realizable k- ϵ	20
3.2.4	Standard k- ω	20
3.2.5	SST k- ω	20
3.3	Computational Domain and Boundary Conditions	21
3.4	Grid Refinement Study.....	25
3.5	Comparison of Turbulence Models	30
3.6	Validation Study at Varying Angles of Attack.....	30
CHAPTER 4 RESULTS AND DISCUSSIONS		33
4.1	Drag Breakdown and Pressure Coefficient Analysis	33
4.2	Flowfield Analysis.....	35
4.2.1	Dimensionless Wall Distance.....	35
4.2.2	Base Model Analysis.....	36
4.2.3	Effect of Angle of Attack	39
4.2.4	Effect of Step Height.....	42
4.2.5	Effect of Sternpost Angle	44
4.2.6	Effect of Deadrise Angle.....	46
4.2.7	Effect of Parameters on Volume of the Fuselage.....	48
4.2.8	Combined Effect of Step Height and Sternpost Angle	49
4.3	Ground Effect	56
4.4	Reynolds Number Effect	57

CHAPTER 5 CONCLUSION AND FUTURE WORK.....	63
REFERENCES.....	65
APPENDIX A MODEL CROSS-SECTIONAL DATA.....	69

LIST OF TABLES

Table 1.1: Notable seaplanes of the early days of the marine aviation	3
Table 2.1: Range of fuselage geometric parameters [20, 21].....	15
Table 3.1: Dimensions of computational domain in meters.....	23
Table 3.2: Ratio of sizing volume dimensions to respective fuselage dimensions	23
Table 3.3: Upstream and downstream lengths of the computational domain in meters	24
Table 3.4: Boundary conditions applied to boundaries of computational domain.....	25
Table 3.5: Results of drag coefficient for varying computational grid resolutions at 0° angle of attack	29
Table 3.6: Comparison of experimental and numerical drag coefficient results obtained at 0° angle of attack using 8.12 million element (fine) grid with various turbulence models	30
Table 4.1: Pressure and viscous drag breakdown of the base model at 0° angle of attack	33
Table 4.2: Drag breakdowns of varying angles of attack.....	40
Table 4.3: Drag coefficient results of angles of attack.....	40
Table 4.4: Drag breakdowns of varying step heights.....	42
Table 4.5: Drag coefficient results of varying step heights.....	42
Table 4.6: Drag breakdowns of varying sternpost angles	44
Table 4.7: Drag coefficient results of varying sternpost angles	44
Table 4.8: Drag breakdowns of varying deadrise angles	46
Table 4.9: Drag coefficient results of varying deadrise angles	47
Table 4.10: Change in fuselage volume with respect to varying fuselage parameters	49
Table 4.11: Values of drag coefficient obtained with varying step heights and sternpost angles	50
Table 4.12: Percent change of drag coefficient obtained with varying step heights and sternpost angles from the base model	50

Table 4.13: Change in fuselage volume with respect to varying step heights and sternpost angles	51
Table 4.14: Percent change in fuselage volume with respect to varying step heights and sternpost angles.....	51
Table 4.15: Wall adjacent cell heights of grids for cases with varying Reynolds Numbers	58
Table 4.16: Drag breakdowns of varying Reynolds Numbers	58
Table 4.17: Effect of Reynolds Number on drag of the base model	58
Table A.1: Offsets for NACA Model 57-A [1]	69

LIST OF FIGURES

Figure 1.1: De Havilland Canada DHC-3 Otter floatplane [7]	4
Figure 1.2: Consolidated PBY Catalina flying boat [8]	5
Figure 1.3: Singular Aircraft Flyox I Amphibious UAV [16]	7
Figure 1.4: A-IHA 12-12-2 Amphibious UAV [17]	8
Figure 2.1: Geometric features shown on a flying boat-type aircraft [20].....	11
Figure 2.2: Geometric features shown on a floatplane-type aircraft [20]	12
Figure 2.3: Geometric parameters shown on front view of NACA 57-A hull CAD model.....	12
Figure 2.4: Geometric parameters shown on back view of NACA 57-A hull CAD model.....	13
Figure 2.5: Geometric parameters shown on side view of NACA 57-A Hull CAD model.....	13
Figure 3.1: View of computational domain, boundaries and sizing volumes (bodies) used to control sizing.....	22
Figure 3.2: View of origin point, inner sizing control volumes and half-fuselage in wireframe mode from symmetry plane	22
Figure 3.3: View of coarser (2.74 million element) grid from symmetry plane	26
Figure 3.4: View of coarse (4.54 million element) grid from symmetry plane	26
Figure 3.5: View of medium (6.33 million element) grid from symmetry plane	26
Figure 3.6: View of fine (8.12 million element) grid from symmetry plane	27
Figure 3.7: View of finer (9.85 million element) grid from symmetry plane	27
Figure 3.8: View of finest (10.44 million element) grid from symmetry plane.....	27
Figure 3.9: Views of the fine grid used for further analyses from symmetry plane ...	28
Figure 3.10: View of grid inflation layer from symmetry plane	29
Figure 3.11: Comparison of drag coefficient values of experimental and numerical results of NACA Model 57-A hull under various angles of attack.....	31
Figure 4.1: Pressure coefficient plot of the base model at 0° angle of attack	34

Figure 4.2: Pressure coefficient plot of the base model at various angles of attack ...	34
Figure 4.3: y^+ distribution on fuselage surface	35
Figure 4.4: Static pressure contours on symmetry plane of NACA Model 57-A hull at 0° angle of attack.....	36
Figure 4.5: Static pressure contours on fuselage surface of NACA Model 57-A hull at 0° angle of attack.....	36
Figure 4.6: Static pressure contours on planes normal to the flow of NACA Model 57-A hull at 0° angle of attack.....	37
Figure 4.7: Streamwise velocity contours on symmetry plane of NACA Model 57-A hull at 0° angle of attack.....	37
Figure 4.8: Streamlines shown on half-fuselage	38
Figure 4.9: Close-up look of streamlines shown on half-fuselage.....	38
Figure 4.10: Contours of streamwise skin friction coefficient indicating flow separation region at the bottom of the NACA Model 57-A hull at 0° angle of attack	39
Figure 4.11: Velocity magnitude contours on symmetry plane of NACA Model 57-A hull at various angles of attack.....	41
Figure 4.12: Streamwise velocity contours for cases with varying step heights.....	43
Figure 4.13: Streamwise skin friction coefficient contours for cases with varying step heights	43
Figure 4.14: Streamwise velocity contours for cases with varying sternpost angles ..	45
Figure 4.15: Streamwise skin friction coefficient contours for cases with varying sternpost angles	46
Figure 4.16: Streamwise velocity contours for cases with varying deadrise angles ...	47
Figure 4.17: Streamwise skin friction coefficient contours for cases with varying deadrise angles	48
Figure 4.18: Streamlines and streamwise velocity contours for the case with 0.513 in step height and varying sternpost angle	52
Figure 4.19: Streamlines and streamwise velocity contours for the case with 0.627 in step height and varying sternpost angle	53

Figure 4.20: Streamlines and streamwise velocity contours for the case with 0.741 in step height and varying sternpost angle54

Figure 4.21: Streamlines and streamwise velocity contours for the case with 0.850 in step height and varying sternpost angle56

Figure 4.22: Drag coefficient trend of varying distances between the bottom of the fuselage and the bottom wall of the domain at 0° angle of attack57

Figure 4.23: Drag coefficient trend of varying flow Reynolds Numbers59

Figure 4.24: Turbulence intensity contours shown on symmetry plane for cases with varying Reynolds Numbers60

Figure A.1: View of cross-sections of NACA Model 57-A model.....70

LIST OF SYMBOLS

α	Angle of Attack
b	Beam Length
C_D	Drag Coefficient
D	Depth
$D_{half-fuselage}$	Depth of Half-Fuselage
Δy	Wall Adjacent Cell Height
δ_{ij}	Kronecker Delta
ε	Turbulent Dissipation
H	Height
$H_{fuselage}$	Height of Fuselage
k	Turbulent Kinetic Energy
L	Length
$L_{fuselage}$	Length of Fuselage
M	Mach Number
μ	Dynamic Viscosity
μ_t	Turbulent Viscosity
ω	Specific Turbulence Dissipation Rate
q	Dynamic Pressure

Re	Reynolds Number
ρ	Density
Tu	Turbulence Intensity
τ_w	Wall Shear Stress
U	Mean Velocity Component
U_∞	Freestream Velocity
u'	Fluctuating Velocity Component
u_τ	Friction Velocity
vol	Volume
y^+	Dimensionless Wall Distance

LIST OF ABBREVIATIONS

ATS	Air Traffic Service
CAD	Computer-Aided Design
CFD	Computational Fluid Dynamics
CPU	Central Processing Unit
DES	Detached Eddy Simulation
DNS	Direct Numerical Simulation
FAA	Federal Aviation Administration
HAER	Historic American Engineering Record Division
IATA	International Air Transport Association
LES	Large Eddy Simulation
NACA	National Advisory Committee for Aeronautics
RANS	Reynolds-Averaged Navier-Stokes
RSM	Reynolds Stress Model
TN	Technical Note
UAV	Unmanned Aerial Vehicle

CHAPTER 1

INTRODUCTION

An amphibious aircraft is defined as an aircraft that can take off from and land on water as well as ground, such as seaplanes equipped with retractable landing gears or hydrofoils, and wing-in-ground-effect aircraft; with most popular of these kinds of aircraft being seaplanes of flying boat types. While widely used in the beginning of modern aviation, seaplane usage declined rapidly afterwards. The fact that seaplanes grew aerodynamically less efficient in time compared to conventional aircraft due to geometric entities they possess for hydrodynamic requirements is considered as the main reason for the deterioration of their usage; as the advantages of their usage over conventional aircraft could not compensate for their relatively higher fuel consumption and lower speed and range. As the runways increased in both availability and length with the end of World War II, and with the development of platforms like radars, helicopters and aircraft carriers, military usage of seaplanes has further diminished.

Nowadays seaplanes are mostly used in countries such as USA, Canada, Greece, Portugal, France, Italy, Spain and Russia for travelling to remote locations with water bodies such as archipelagos, firefighting, marine search and rescue missions and recreational purposes. The recent progress in seaplanes and UAV's and in development of corrosion-resistant composite materials, and the rapid increase in air traffic on and around proximity of runways show potential for amphibious aircraft to be widely used again in the future [1-4].

1.1 Historical Background

The idea for building a flying machine that can take-off from and land on water goes as far back as 1876, to aviation pioneer Alphonse Pénau's patent with a boat hull and a retractable landing gear mounted under its wings. In 1897, Edson Fessenden Gallaudet built Gallaudet Hydroplane, an unpiloted glider featuring twin floats. Drachenflieger, the first motor seaplane was built by Wilhelm Kress in 1901, but was unable to take-off successfully due to the poor power-to-weight ratio of its engine. In 1905, Gabriel Voisin became the first person to take-off from and land on water with the unpowered glider he designed and built being towed by a motor boat on river Seine.

Seven years after the first controlled, powered, heavier-than-air flight by Wright brothers; on 28 March 1910, Henri Fabre designed and piloted the world's first seaplane Hydravion (French for seaplane), a trimaran floatplane, to successfully take-off from and land on Étang de Berre lagoon at Martigues, France.

After the success of Hydravion, marine aviation began advancing rapidly, with designers such as Henri Fabre, Glenn Curtiss, Henri Farman and Alphonse Tellier developing various floats and several proven aircrafts being fitted with floats. Canard Voisin became the first seaplane used from a seaplane carrier, La Foudre (French for lightning), the first seaplane carrier. This was followed by Monaco 1912, first seaplane competition arranged for the purpose of demonstrating capabilities of seaplanes and generating interest for research, and first regular passenger transportation services with a seaplane by Compagnie Générale Transaérienne. French navy also ordered its first seaplane in 1912.

The first flying boat with a fuselage shaped as a ship's hull, designed by François Denhaut has also made its maiden flight in 1912; and incorporated a step at the bottom of the hull to reduce contact with the water to achieve the take-off speed required, which was also demonstrated in Glenn Curtiss' Flying Fish amphibious aircraft [5, 6].

Table 1.1: Notable seaplanes of the early days of the marine aviation

Seaplane	Designer	First Flight
Hydravion	Henri Fabre	1910
Canard Voisin	Gabriel Voisin, Charles Voisin	1911
Poisson Volant	François Denhaut	1912
Flying Fish	Glenn Curtiss	1912
Sánchez Besa biplane	José Luis Sánchez Besa	1912
Astra C	Société Astra	1912
Borel monoplane	Gabriel Borel	1912
Henri Farman biplane	Henri Farman	1912

During the Balkan Wars, a Greek Astra Hydravion became the first seaplane conducting a combat mission, engaging in reconnaissance of the Turkish fleet and dropping four bombs before landing on sea near Gökçeada. World War I period also saw intensive development and use of seaplanes, used in coastal and sea patrols. The first transatlantic flight was made by a seaplane in 1919, a U.S. Navy Curtiss NC-4, and was followed with the introduction of commercial seaplane passenger and mail transportation services.

During World War II, seaplanes were abundant and were used in a variety of tasks, such as anti-submarine warfare, patrol-bombing, air-sea rescue, cargo transportation and convoy escorting. The most widely used and produced flying boat of the era, Consolidated PBY Catalina, and the largest flying boat ever built, also having the largest wingspan of any aircraft in history, the prototype Hughes H-4 Hercules (also known as “Spruce Goose”) were both developed in this period.

After the end of World War II, significant investments were made to improve the airfield infrastructure around the world. The number and length of runways have greatly increased, and the further progress on land based aircraft improved the speed and range limits of the aircrafts, rendering seaplane usage superfluous except limited

necessities. With development of platforms such as radars and helicopters, and advances on aircraft careers, military usage of seaplanes also declined drastically.

1.2 Literature Survey

Amphibious aircraft can be divided into two categories depending on their shapes of fuselages as floatplanes and flying boats. Floatplanes have floats (also called pontoons) mounted under their fuselage that provide buoyancy, while flying boats have fuselages designed as hulls for the purpose of granting buoyancy and moving through water. Many amphibious aircraft have flying boat type fuselages, which is also well suited for unmanned operations due to their tendency of having lower drag, better stability on water and lower empty weight compared to floatplanes; and lack of need for boarding the aircraft on water [6].

Aircraft of both categories are shown in Figure 1.1 and Figure 1.2, respectively.



Figure 1.1: De Havilland Canada DHC-3 Otter floatplane [7]



Figure 1.2: Consolidated PBY Catalina flying boat [8]

Flying boat fuselages and floatplane floats have been very similar in shape, and other than the step and the sternpost angle, similar with high-speed planing boats such as speedboats; and they possess the same geometric entities at the lower half of their structures due to being exposed to same hydrodynamic and aerodynamic effects. Various models of both have been extensively studied by NACA (National Advisory Committee for Aeronautics), especially in 1930's and 1940's by means of towing tank and wind tunnel experiments, for the purposes of determining hydrodynamic and aerodynamic characteristics, respectively, and reducing aerodynamic drag without affecting hydrodynamic performance [9].

Prediction of drag has always been one of the most important and complex areas in the field of fluid mechanics, and has been widely studied both theoretically and experimentally. Similarly, prediction and reduction of aerodynamic drag for the purpose of designing highly efficient aircraft has been crucial for aircraft manufacturers, who must ensure the performance of the aircraft is conforming to requirements, in terms such as fuel consumption, speed, range and payload. Experimental studies, namely wind tunnel techniques have always been the main tools for accurate measurement of drag of aircraft. Development of numerical methods such

as CFD codes provided a practical and cost-effective alternative, and proved especially useful for evaluating different configurations that are large in amount [10, 11].

Aerodynamic drag of bodies subjected to airflow is greatly affected by the following factors [12]:

- Skin friction drag, occurring due to viscous effects in boundary layers
- Induced drag, resulting from generation of lift at lifting surfaces
- Pressure drag, acting on the body due to separation at the wake
- Interference drag occurring due to interference of flows around different components with each other
- Wave drag generated due to compressibility effects
- Other effects, such as roughness and leakage

The accurate prediction of drag components mentioned above by using modern CFD methods depend on several factors, such as [13]:

- Accurate representation of the geometry of interest
- Adequate size and density of the computational grid
- Numerical solving techniques adapted
- Modelling turbulence to provide satisfactory results
- Convergence of numerical solution
- Prediction of flow phenomena such as transition and separation

1.3 Motivation for the Study

Due to lack of demand, research and development of amphibious aircraft have been largely abandoned, and their usage is significantly diminished other than the activities and necessities mentioned previously, such as geographical isolation and lack of runways. Considering the advantages of unmanned operations over manned operations, such as lower risk to humans and higher mission confidence, UAV's are expected to replace manned aircraft in the near future. Some of the proposed civil and commercial

applications of UAV's are security awareness, disaster response with search and support to rescuers, communications and broadcast, cargo transport, spectral and thermal analysis, critical infrastructure monitoring including power facilities, ports, and pipelines, commercial photography, aerial mapping and charting, and advertising. Firefighting and oceanographic studies can be named for other applications specific to amphibious UAV's [14, 15].

Figure 1.5 below shows Singular Aircraft Flyox I, an amphibious UAV which was designed with four different configurations for agricultural, firefighting, surveillance & lifesaving, and cargo transportation purposes; and Figure 1.6 shows A-IHA 12-12-2 amphibious UAV used for remote sensing of water quality parameters.



Figure 1.3: Singular Aircraft Flyox I Amphibious UAV [16]



Figure 1.4: A-IHA 12-12-2 Amphibious UAV [17]

In addition from a general aviation viewpoint, current overload of airports and ATS (Air Traffic Service) routes (air ways, designated routes for the flow of traffic), and the ever increasing traffic in addition to rapid growth of number of UAV's could benefit from the potential of amphibious aircraft. The usage of amphibious UAV's for missions conducted by land-based aircraft could help in reducing the air traffic, especially in countries such as Turkey, where hundreds of well suited small and large water bodies are present. Currently there are 83 locations designated to the use of seaplanes to depart from and arrive on by Turkish Directorate General of Civil Aviation [18].

The motivation for the study is to investigate the amphibious UAV's from an aerodynamic point of view for the purpose of determining and improving the aerodynamic efficiency by making use of modern analysis methods, namely CFD, to narrow the amount of performance gap with the conventional aircraft.

1.4 Purpose of the Study

Although wind tunnels are still the cornerstones for designing and developing objects that are subjected to strong air flow as they were back in 1800s, computational methods have emerged in the latter part of the 20th century, and have been continuing to progress at a great pace since then. Nowadays CFD is an important tool for such practices, accurately able to predict and analyze the aerodynamic behavior of bodies subject to fluid flow, and is especially useful when the quantity of samples needed to be analyzed increase.

The purpose of this study is to investigate the effect of changing geometric parameters of a hull-shaped fuselage, which are commonly found in amphibious aircrafts, on aerodynamic drag of the body; to obtain useful data regarding the aerodynamic performance of an aerial vehicle that incorporates such geometries and insight of the physics of the flow by means of CFD. For this purpose, accuracy of the computational method was needed to be measured, and the computational data obtained using various grid densities and turbulence models were compared to wind tunnel results of the bodies to ensure adequate accuracy without exorbitant consumption of CPU time.

CHAPTER 2

DESIGN PARAMETERS

2.1 Hull Shape Parameters

Amphibious aircraft operate on water as well as air and land, therefore their performance is highly dependent on the optimization of their shape. Shape of the fuselage is constrained by hydrodynamic performance requirements needed for safe take-off and landing, which in turn affects the aerodynamic performance of the aircraft, especially at cruise condition [19, 20].

Geometric features of flying boat-type and floatplane-type aircrafts are shown in Figure 2.1 and Figure 2.2, and geometric parameters of a generic amphibious aircraft fuselage are shown on front, back and side views of the CAD model of NACA Model 57-A Hull in Figure 2.3 to Figure 2.5 [1, 20].

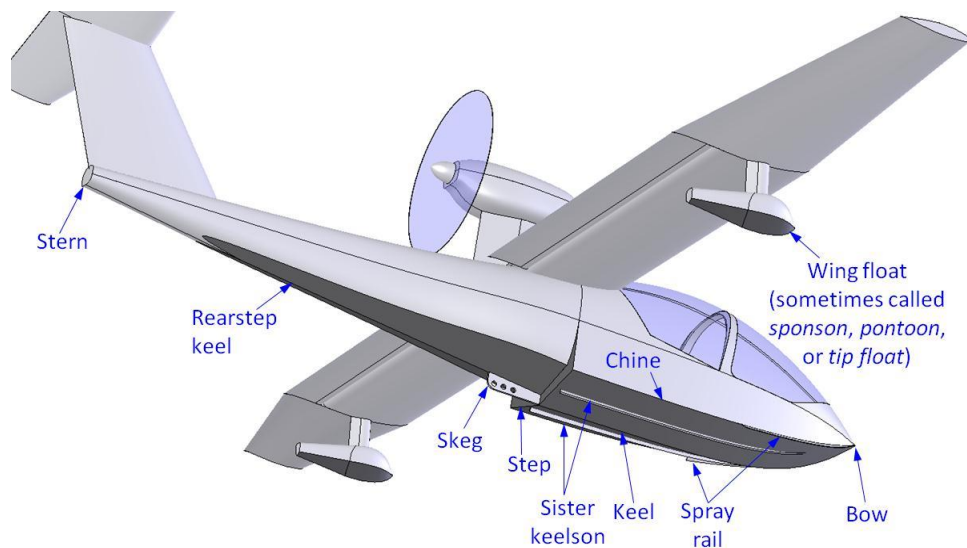


Figure 2.1: Geometric features shown on a flying boat-type aircraft [20]

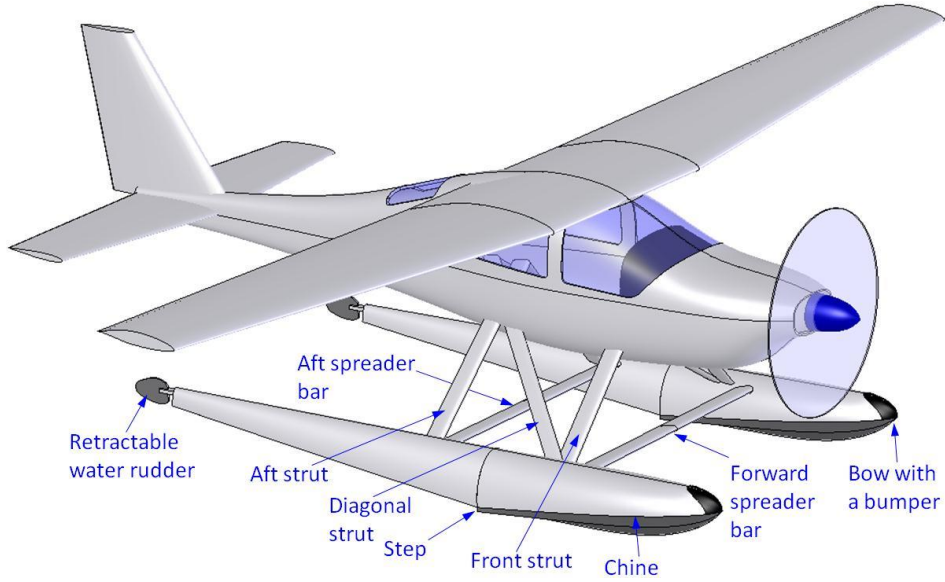


Figure 2.2: Geometric features shown on a floatplane-type aircraft [20]

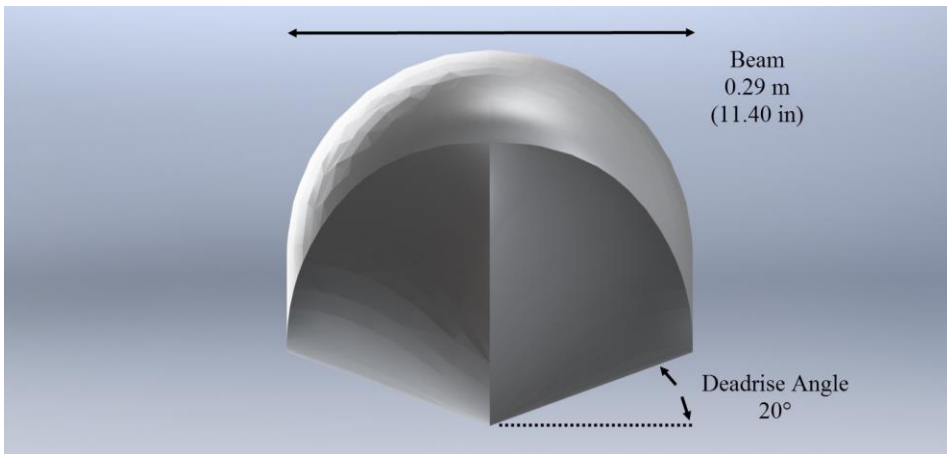


Figure 2.3: Geometric parameters shown on front view of NACA 57-A hull CAD model

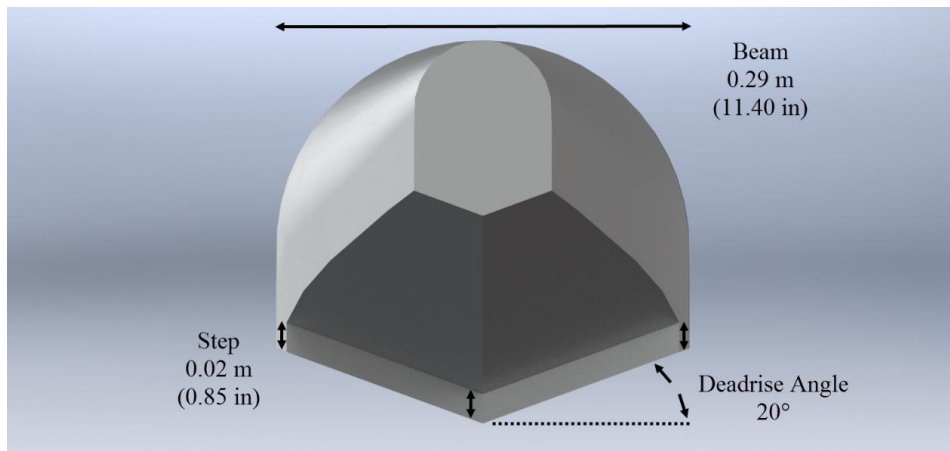


Figure 2.4: Geometric parameters shown on back view of NACA 57-A hull CAD model

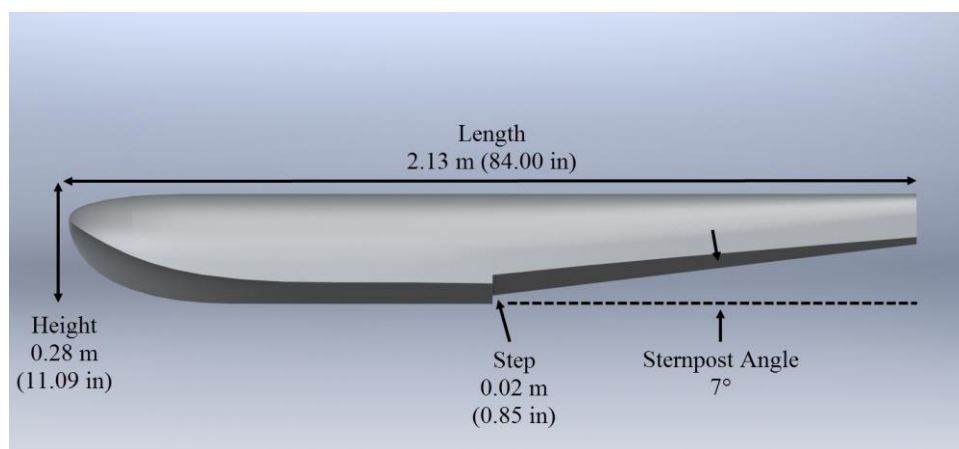


Figure 2.5: Geometric parameters shown on side view of NACA 57-A Hull CAD model

The NACA 57-A Hull model is selected as the base model for which the effects of the changes in angle of attack and in the following parameters have on the drag of the body are investigated.

2.1.1 Step

Step is the vertical discontinuity located at the bottom of the hull, required to break contact with water and overcome hydrodynamic drag occurring due to vacuum of the water during take-off. This suction generated by the adhesion of the water increases with the increase in speed of the aircraft. Step allows to control the pitch of the aircraft by creating a region of air that the aircraft “planes” on just like a speedboat, reducing the wetted area that is in contact with the water and in turn hydrodynamic drag, allowing the aircraft to take-off. Therefore steps are generally located close, slightly aft to the center of gravity of the aircraft to allow for easier control of the pitch angle.

Since step is a discontinuity on the streamlined shape of the fuselage, it comes with a decrease in aerodynamic performance. Eddies forming in the step region increases pressure drag, thus decreases aerodynamic efficiency of the aircraft. Therefore it is important that the step is designed to provide a balance between hydrodynamic and aerodynamic performance [4, 19, 20].

2.1.2 Deadrise Angle

Deadrise angle is the upward angle from horizontal of the traditional “V” shaped hull bottom that is needed to reduce water impact loads and provide directional stability. Although it is favorable to increase the deadrise angle to lower the hull impact loadings and in turn, reduce the weights associated with structural requirements, since it is an important design consideration that determines the amount of the fuselage that stays under the waterline, it should be ensured to be optimized [4, 19, 20].

2.1.3 Sternpost Angle

Sternpost angle is the angle that the rear section of the fuselage makes with the horizontal, needed to avoid contact with the water during take-off. Sternpost angle accounts for the pitch-up angle of the planing aircraft to ensure the aft of the fuselage

does not contact water, which would further increase the hydrodynamic drag and increase take-off distance of the aircraft [19, 20].

2.1.4 Other Parameters

Other design parameters include beam length, which is the widest section of the hull; length to beam ratio, which affects the cross-sectional area and in turn, aerodynamic and hydrodynamic drag of the body; forebody and afterbody lengths that determine stability and planing characteristics of the aircraft; and hull bottom shape that determines hull impact loading, water spray and body wetted area under waterline. Since these parameters also directly affect the design and performance of the aircraft, they should be determined with general and mission-specific design requirements in mind [4, 19, 20].

2.1.5 Typical Ranges of Design Parameters

Typical ranges of parameters obtained from literature are given in Table 2.1, which were established through experimentation and empirical models for the design of amphibious aircrafts [19, 20].

Table 2.1: Range of fuselage geometric parameters [20, 21]

Fuselage Parameter	Range
Step Height	4% to 8% of beam
Deadrise Angle	15° to 40°
Sternpost Angle	7° to 9°

To investigate the effects of such parameters on cruise drag, CFD analyses have been conducted on a CAD model generated using SolidWorks CAD software of a generic

hull shape (NACA Model 57-A) described in NACA Technical Note No. 716. The models were created by extrapolating available data of cross-sectional dimensions given in the technical note.

2.2 Analytical Model for Drag Coefficient

Drag coefficient is defined with the following relationship:

$$C_D \equiv \frac{D}{q(vol)^{2/3}} \quad (2.1)$$

Where C_D is the drag coefficient, D is the drag force, vol is the volume of the body, and q is the dynamic pressure, defined as the following:

$$q = \frac{1}{2} \rho U_\infty^2 \quad (2.2)$$

Here, ρ denotes the density of the fluid, and U_∞ denotes the freestream velocity. In Equation 2.1, square of the cube root of the volume of the fuselage is used instead of the area due to volume of the fuselage being an independent design variable.

Drag coefficient is obtained from Equation 2.1, with the drag force found by integration of inertial and viscous forces acting on the body, obtained from numerically solved flow field data. The methodology of the computational method is explained in Chapter 3 in detail [1].

CHAPTER 3

COMPUTATIONAL METHOD

3.1 Governing Equations

The Reynolds-Averaged Navier-Stokes (RANS) equations used to define fluid motion in turbulent flows, with mean and fluctuating flow quantities represented in tensor notation are given for incompressible flows in Equation 3.1 and Equation 3.2;

$$\frac{\partial \rho}{\partial t} + \frac{\partial}{\partial x_i} (\rho u_i) = 0 \quad (3.1)$$

$$\begin{aligned} \frac{\partial}{\partial t} (\rho u_i) + \frac{\partial}{\partial x_j} (\rho u_i u_j) = & -\frac{\partial p}{\partial x_i} + \\ \frac{\partial}{\partial x_j} \left[\mu \left(\frac{\partial u_i}{\partial x_j} + \frac{\partial u_j}{\partial x_i} - \frac{2}{3} \delta_{ij} \frac{\partial u_l}{\partial x_l} \right) \right] + & \frac{\partial}{\partial x_j} (-\rho \overline{u'_i u'_j}) \end{aligned} \quad (3.2)$$

where u is the velocity, ρ is the density of the fluid, p is the pressure, and μ is the dynamic viscosity. Here, flow quantities are decomposed to mean and fluctuating components, such that;

$$u_i = \bar{u}_i + u'_i \quad (3.3)$$

for velocity and

$$\phi = \bar{\phi} + \phi' \quad (3.4)$$

for scalar quantities. Here, the non-linear Reynolds stress term $-\rho \overline{u'_i u'_j}$ in Equation 3.2 needs to be modeled in order to overcome the closure problem arising from the lack of equations needed to solve for the unknowns. Together by applying the Boussinesq approximation;

$$-\rho \overline{u_i' u_j'} = \mu_t \left(\frac{\partial u_i}{\partial x_j} + \frac{\partial u_j}{\partial x_i} \right) - \frac{2}{3} \left(\rho k + \mu_t \frac{\partial u_k}{\partial x_k} \right) \delta_{ij} \quad (3.5)$$

where μ_t is the turbulent viscosity considered as a flow property, k is the turbulent kinetic energy, and δ_{ij} is the Kronecker delta; Reynolds stress term is modeled using one-equation and two-equation turbulence models described below briefly [22, 23].

3.2 Turbulence Modelling

Various models are used for modelling the turbulent flows in the study, which have been extensively studied in the literature and has been found to perform very well for similar flows, with different strengths and weaknesses. These models are briefly described in the following sections, in the form implemented to the CFD code, as discussed in ANSYS Fluent Theory Guide that is the main reference for this section [23].

The referred number of equations of the models are the additional differential equations that are solved along with the RANS equations. Among turbulence models, three have been widely used and validated, and considered the most practical with similar aerodynamic problems due to their robustness, accuracy and time-wise and resource-wise economy, being Spalart-Allmaras (one-equation model), k- ϵ (two-equation model) and k- ω (two-equation model) based turbulence models. Zero-equation models (e.g. Mixing Length) were not applicable to the study due to the complexity of the flow, and higher order models (e.g. RSM (Reynolds Stress Model), DES (Detached Eddy Simulation), LES (Large Eddy Simulation) and DNS (Direct Numerical Simulation)) were not applicable due to their high consumption of time and computational resources.

3.2.1 Spalart-Allmaras

Spalart-Allmaras model is a one-equation turbulence model, developed for aerodynamic flows and has shown to perform well with boundary layers with adverse pressure gradients, that turbulent viscosity is modelled with one transport equation.

Essentially Spalart-Allmaras model requires the boundary layer to be modelled down to the level of viscous sublayer (viscosity dominated region of the boundary layer that is in contact with the rigid wall), therefore a dimensionless wall distance, y^+ of 1 is used. With a y^+ insensitive wall treatment, however, the model can be implemented to use for larger values of y^+ by automatically applying the law of the wall at the logarithmic region of the boundary layer, where the viscous effects are no longer dominant to inertial effects.

Dimensionless wall distance, y^+ is defined as the following:

$$y^+ = \frac{yu_\tau}{\nu} \quad (3.6)$$

Here, y is the distance to the wall, ν is the dynamic viscosity of the fluid and u_τ is the friction or shear velocity, defined in Equation 3.7 below.

$$u_\tau \equiv \sqrt{\frac{\tau_w}{\rho}} \quad (3.7)$$

3.2.2 Standard k-ε

Standard k-ε is a two-equation semi-empirical turbulence model that incorporates two transport equations for k (which is the turbulent kinetic energy equation) and ε , where ε is the turbulent dissipation.

Since standard k-ε model relies on the assumption that the effects of molecular viscosity is negligible, it is applicable to fully turbulent flows only; however it was

shown to produce good results for a large variety of cases, making it an industry standard since its emergence.

3.2.3 Realizable k- ϵ

Realizable k- ϵ model is considered an improvement on the standard k- ϵ with a different approach to determine turbulent viscosity, and a revised transport equation for the turbulent dissipation that is derived directly from equation of the mean-square vorticity fluctuation transport. It is known to provide good results for a variety of flows, including flows with strong streamline curvature, vortices, and rotation making this model superior to the Standard k- ϵ especially in flows with such phenomenon; and has been shown to perform best of all k- ϵ models in cases with separated flows and flows with complex secondary flow features.

3.2.4 Standard k- ω

Standard k- ω is a two-equation empirical turbulence model that instead of a transport equation for ϵ , incorporates the transport equation for the ratio of ϵ to k , called specific turbulence dissipation rate, or turbulence frequency:

$$\omega = \frac{\epsilon}{k} \quad (3.8)$$

A common disadvantage of the model is the freestream sensitivity that is the accuracy of the solution is dependent on the freestream turbulence properties k and ω .

3.2.5 SST k- ω

SST (Shear Stress Transport) $k-\omega$ is a refinement of the standard $k-\omega$ to take advantage of near-wall accuracy of $k-\omega$ models and the accuracy of the $k-\varepsilon$ models outside the shear layer. The freestream accuracy is obtained by incorporating a blending function to use a transformed $k-\varepsilon$ formulation away from surface, and the standard $k-\omega$ formulation in the near-wall region.

It is known to provide good results for such flows with adverse pressure gradients, separating flows and transonic shock waves.

3.3 Computational Domain and Boundary Conditions

Computational domain is shown on Figure 3.1 and Figure 3.2, and dimensions of computational domain are given in Table 3.1 and Table 3.2. Aside from the rectangular computational domain, several sizing volumes were defined to control the sizing of the elements that lay within, to increase grid resolution where gradients of local flow quantities are greater in comparison to gradients in the outer regions of the domain.

Since the fuselage geometry is symmetrical with respect to xy -plane, computational domain was selected as one half of the initial domain, cut in half from the xy -plane (symmetry plane) to reduce the number of elements and thus, to reduce the computational expense of the analyses. Calculated values of drag were then multiplied by two to obtain the drag of the full body. Drag and drag coefficient results given in the following sections are respective full body values.

Although enclosure and sizing volume edges are symmetrical on y and z axes with respect to origin point; to account for and better capture the wake effects on the downstream flow field, computational domain and the sizing volumes are extended through downstream x direction. Upstream and downstream lengths are given in Table 3.3.

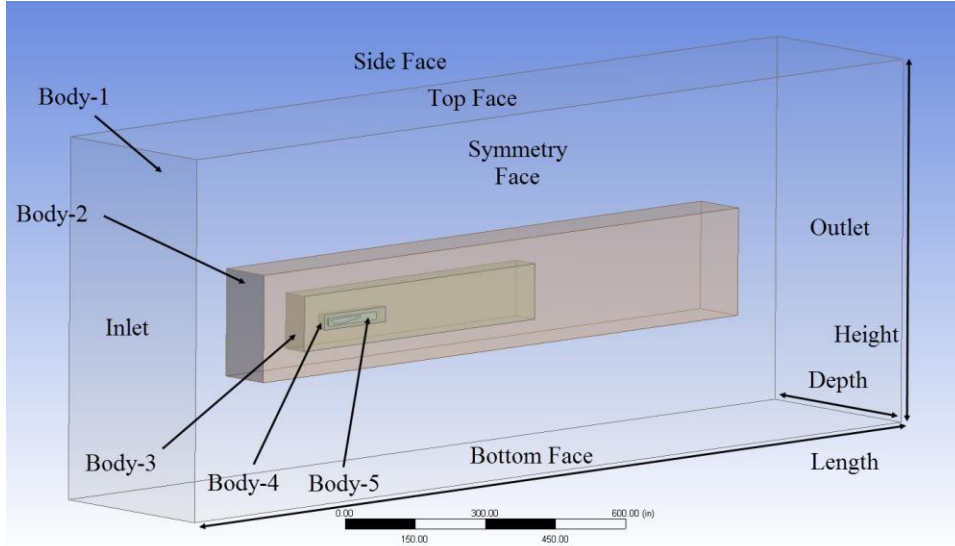


Figure 3.1: View of computational domain, boundaries and sizing volumes (bodies) used to control sizing

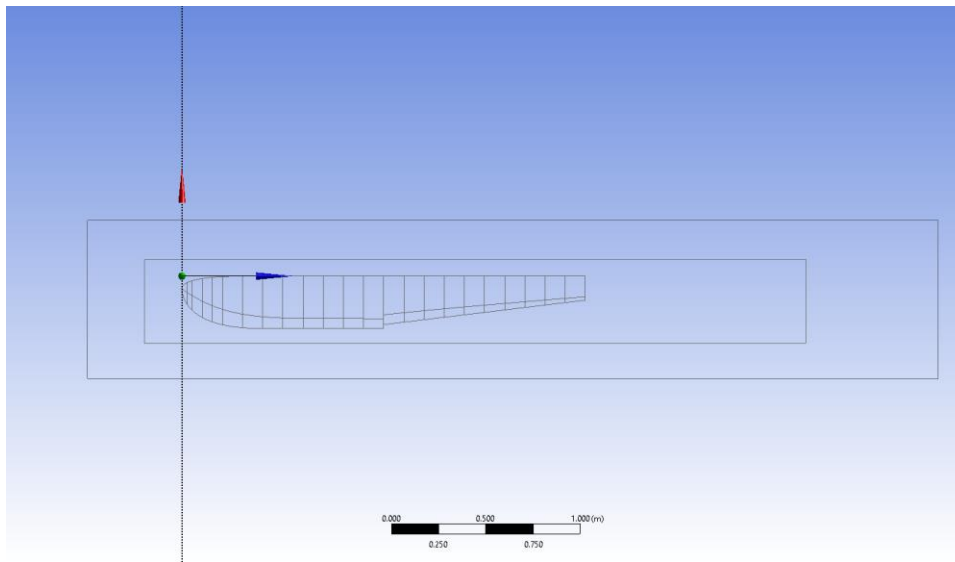


Figure 3.2: View of origin point, inner sizing control volumes and half-fuselage in wireframe mode from symmetry plane

Table 3.1: Dimensions of computational domain in meters

	L	H	D
Body-1 (Comp. Domain Enclosure)	50.00 m	20.00 m	10.00 m
	1968.50 in	787.40 in	393.70 in
Body-2 (Outermost Sizing Control Vol.)	35.00 m	6.00 m	3.00 m
	1377.95 in	236.22 in	118.11 in
Body-3 (Outer Sizing Control Vol.)	17.00 m	3.10 m	1.50 m
	669.29 in	122.05 in	59.06 in
Body-4 (Inner Sizing Control Vol.)	4.50 m	0.85 m	0.50 m
	177.17 in	33.46 in	19.69 in
Body-5 (Innermost Sizing Control Vol.)	3.50 m	0.45 m	0.15 m
	137.80 in	17.72 in	5.91 in
Half-Fuselage	2.13 m	0.28 m	0.14 m
	84.00 in	11.09 in	5.70 in

Table 3.2: Ratio of sizing volume dimensions to respective fuselage dimensions

	L/L_{fuselage}	H/H_{fuselage}	$D/D_{\text{half-fuselage}}$
Body-1 (Comp. Domain Enclosure)	23.43	71.00	69.07
Body-2 (Outermost Sizing Control Vol.)	16.40	21.30	20.72
Body-3 (Outer Sizing Control Vol.)	7.97	11.01	10.36
Body-4 (Inner Sizing Control Vol.)	2.11	3.02	3.45
Body-5 (Innermost Sizing Control Vol.)	1.64	1.60	1.04
Half-Fuselage	1	1	1

Table 3.3: Upstream and downstream lengths of the computational domain in meters

	L_{upstream}	$L_{\text{downstream}}$
Body-1 (Comp. Domain Enclosure)	10.00 m 393.70 in	40.00 m 1,574.80 in
Body-2 (Outermost Sizing Control Vol.)	5.00 m 196.85 in	30.00 m 1,181.10 in
Body-3 (Outer Sizing Control Vol.)	2.00 m 78.74 in	15.00 m 590.55 in
Body-4 (Inner Sizing Control Vol.)	0.50 m 19.69 in	4.00 m 157.48 in
Body-5 (Innermost Sizing Control Vol.)	0.20 m 7.87 in	3.30 m 129.92 in
Half-Fuselage	-	2.13 m 84.00 in

Velocity Inlet with a magnitude of 35.78 m/s (80.04 mph), Pressure Outlet corresponding to atmospheric pressure, Symmetry, Slip Wall and No-slip Wall boundary conditions were applied to relevant boundaries of computational domain to obtain the experimental dynamic pressure of 783.80 Pa (16.37 lbf/ft²) with the air density of 1.225 kg/m³, which results in a flow Reynolds Number of 5.2×10^6 and a Mach Number of 0.1, obtained from below relations given in Equation 3.9 and Equation 3.10, respectively [1].

$$Re = \frac{\rho U_{\infty} L}{\mu} \quad (3.9)$$

$$M = \frac{U_{\infty}}{c} \quad (3.10)$$

Here, Re is the non-dimensional Reynolds Number, ρ is the air density, L is the characteristic length, μ is the dynamic viscosity of air; and M is the Mach Number, U_∞ is the air velocity, and c is the speed of sound at air.

Boundary conditions are listed below in Table 3.4.

Table 3.4: Boundary conditions applied to boundaries of computational domain

Boundary	Boundary Condition	Value
Inlet	Velocity Inlet	35.78 m/s
Outlet	Pressure Outlet	101.325 kPA
Symmetry Face	Symmetry	-
Top, Side, Bottom Faces	Slip (Zero-Shear) Wall	-
Half-Fuselage	No Slip Wall	-

3.4 Grid Refinement Study

A refinement study of the computational grid has been performed, in which the elements located within the sizing control volumes being lowered in size gradually with each refinement level. The non-dimensional wall distance of elements adjacent to the fuselage surface was held constant as $y_{max}^+ \approx 1$ in each step to resolve the boundary layer to the viscous sublayer, and the grid inflation layer covering the boundary layer thickness throughout the fuselage surface consisted of 55 layers, growing in size in the direction normal to the boundary with a growth rate of 1.1. This resulted in a grid with structured wedge elements at the inflation layer, with a wall adjacent cell distance in the direction normal to the boundary (Δy) of 0.01108 mm (0.00044 in); and unstructured tetrahedral elements at the outer regions of the computational domain.

It was observed that the computational grid consisting of 8.12 million elements has proved adequate accuracy without exorbitant CPU time, and has been used for further analyses. View of computational grids of varying resolutions from symmetry plane are

given in Figure 3.3 to Figure 3.8, and view of fine grid used in further analyses and the respective grid inflation layers are given in Figure 3.9 and Figure 3.10 below. Drag coefficient results of grid refinement study is given in Table 3.5.

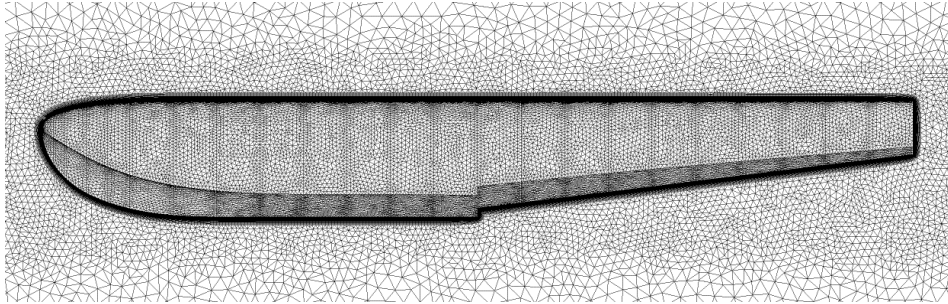


Figure 3.3: View of coarser (2.74 million element) grid from symmetry plane

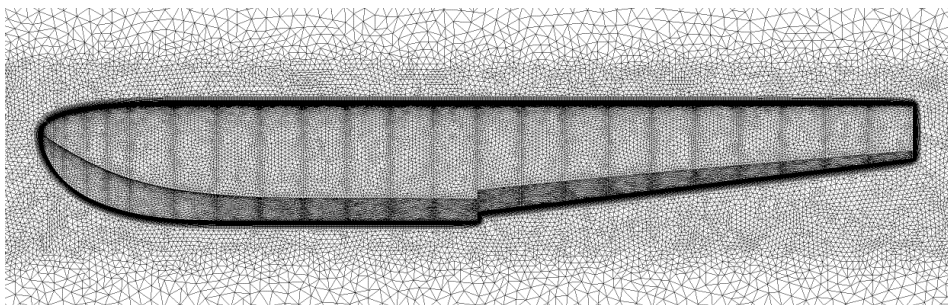


Figure 3.4: View of coarse (4.54 million element) grid from symmetry plane

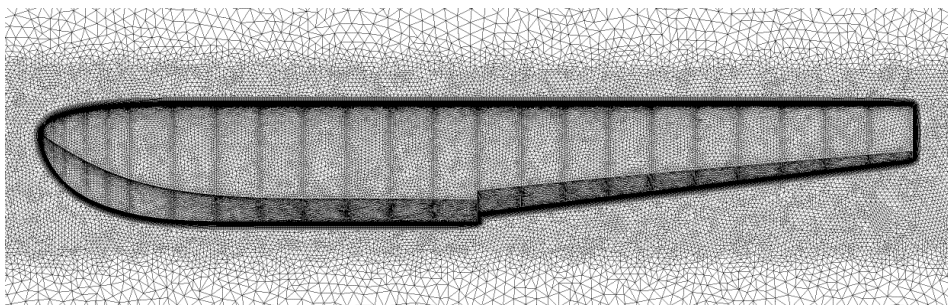


Figure 3.5: View of medium (6.33 million element) grid from symmetry plane

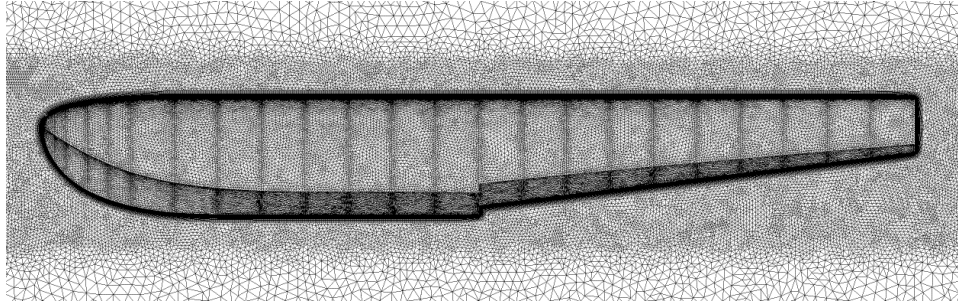


Figure 3.6: View of fine (8.12 million element) grid from symmetry plane

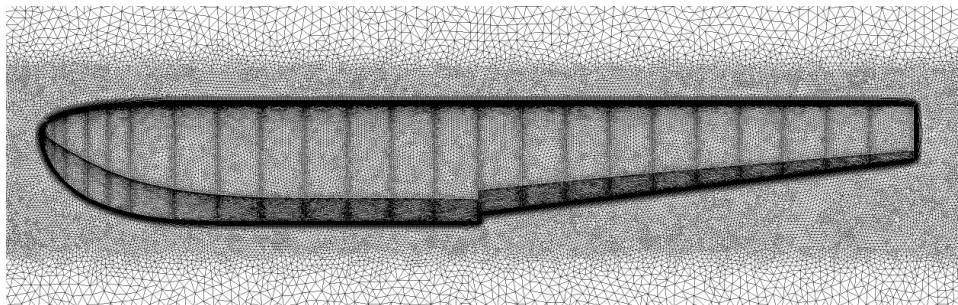


Figure 3.7: View of finer (9.85 million element) grid from symmetry plane

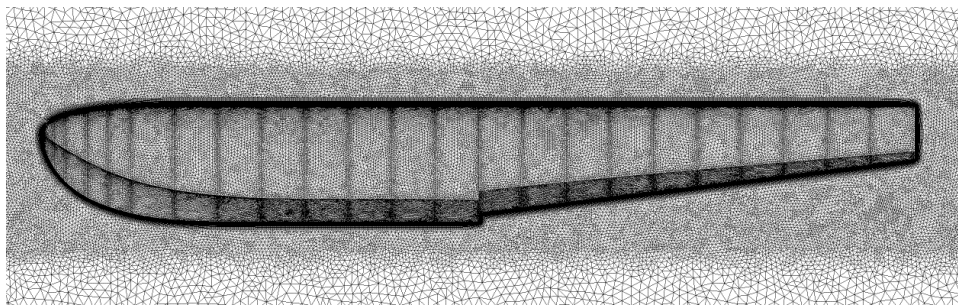


Figure 3.8: View of finest (10.44 million element) grid from symmetry plane

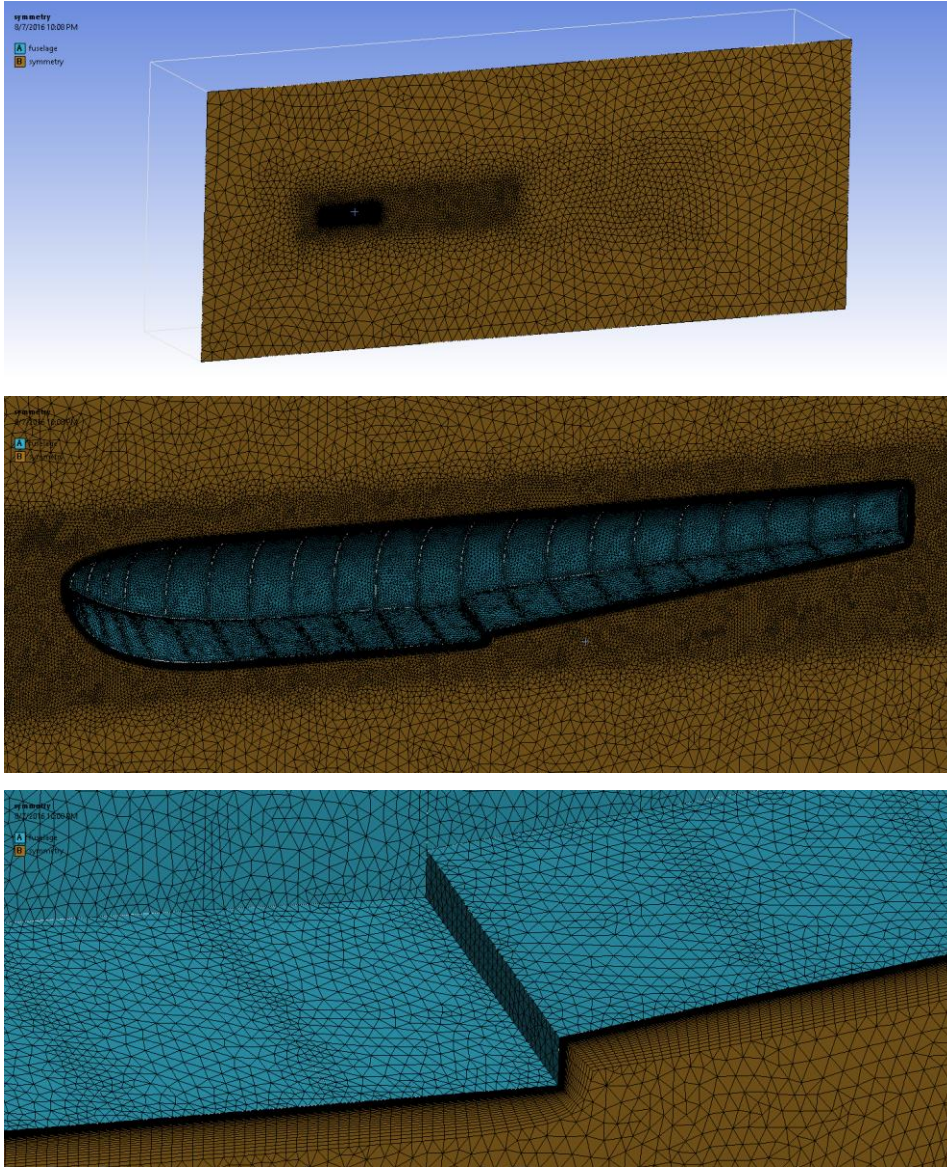


Figure 3.9: Views of the fine grid used for further analyses from symmetry plane

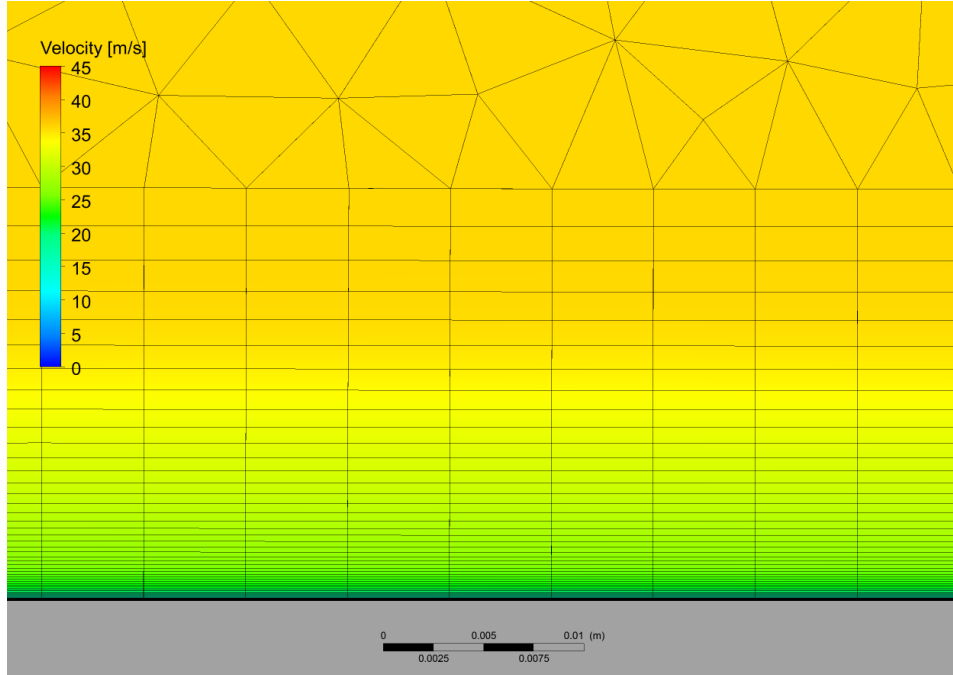


Figure 3.10: View of grid inflation layer from symmetry plane

Table 3.5: Results of drag coefficient for varying computational grid resolutions at 0° angle of attack

Grid Resolution (Million Elements)	C_D
Coarser (2.74)	0.04830
Coarse (4.54)	0.04667
Medium (6.33)	0.04591
Fine (8.12)	0.04523
Finer (9.85)	0.04499
Finest (10.44)	0.04487
Experimental (NACA-TN-716)	0.04101

3.5 Comparison of Turbulence Models

Measured values of drag coefficient given in NACA Technical Note No. 716 was compared to numerical results obtained from commercial CFD code ANSYS Fluent 3D RANS solver under steady-state, incompressible flow assumptions; and by using Spalart-Allmaras, SST $k-\omega$ and Realizable $k-\epsilon$ turbulence models, which have been widely applied for analyses of a wide range of flows. Aerodynamic tests described in NACA Technical Note No. 716 were conducted in NACA Langley 7-by-10-foot Wind Tunnel, which had an open test chamber with a cross-section of 2.13 x 3.05 m [1, 24].

Comparison of various turbulence models used is shown in Table 3.6 below.

Table 3.6: Comparison of experimental and numerical drag coefficient results obtained at 0° angle of attack using 8.12 million element (fine) grid with various turbulence models

Turbulence Model	C_D
Realizable $k-\epsilon$	0.06510
Spalart-Allmaras	0.05025
SST $k-\omega$	0.04523
Experimental (NACA-TN-716)	0.04101

It was seen that the case with SST $k-\omega$ implemented as the turbulence model agreed best with the experimental results, as expected in flows with strong separation, and has been implemented in further analyses.

3.6 Validation Study at Varying Angles of Attack

Analyses for validation study were performed at angles of attack ranging between -8° and 16° for base model to compare numerical results with the experimental results given in NACA Technical Note No. 716. Results are shown below in Figure 3.11,

where black markers denote experimental values and blue markers denote numerical values at respective angles of attack.

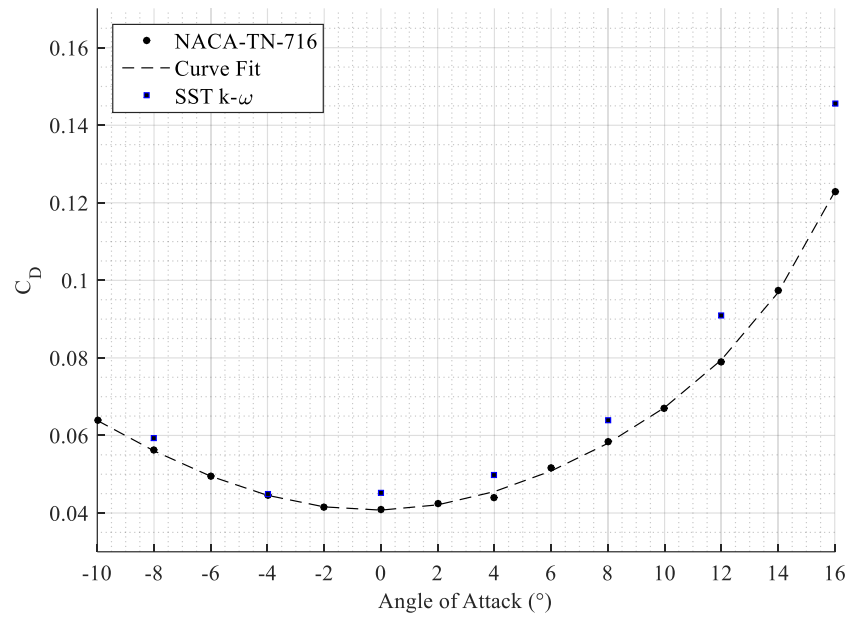


Figure 3.11: Comparison of drag coefficient values of experimental and numerical results of NACA Model 57-A hull under various angles of attack

CHAPTER 4

RESULTS AND DISCUSSIONS

4.1 Drag Breakdown and Pressure Coefficient Analysis

In this section, pressure and viscous components of the drag force that the flow exerts on the body is calculated for the purpose of determining their relative effects on the total drag of the body.

Drag breakdown of the base model at 0° angle of attack is given below in Table 4.1.

Table 4.1: Pressure and viscous drag breakdown of the base model at 0° angle of attack

Drag	Pressure	Viscous	Total
Drag Force (N)	3.66	3.84	7.50
C_D	0.02210	0.02314	0.04523
Experimental C_D			0.04101

As shown in Table 4.1, the pressure and the viscous drag is affecting the fuselage about evenly, thus efforts for reducing both pressure and viscous drag to improve aerodynamic efficiency of the body is viable, and should both be given emphasis.

Pressure coefficient plot of base model at 0° angle of attack on fuselage symmetry plane, and comparison of pressure coefficient plots obtained for various angles of attack are given below in Figure 4.1 and Figure 4.2, respectively.

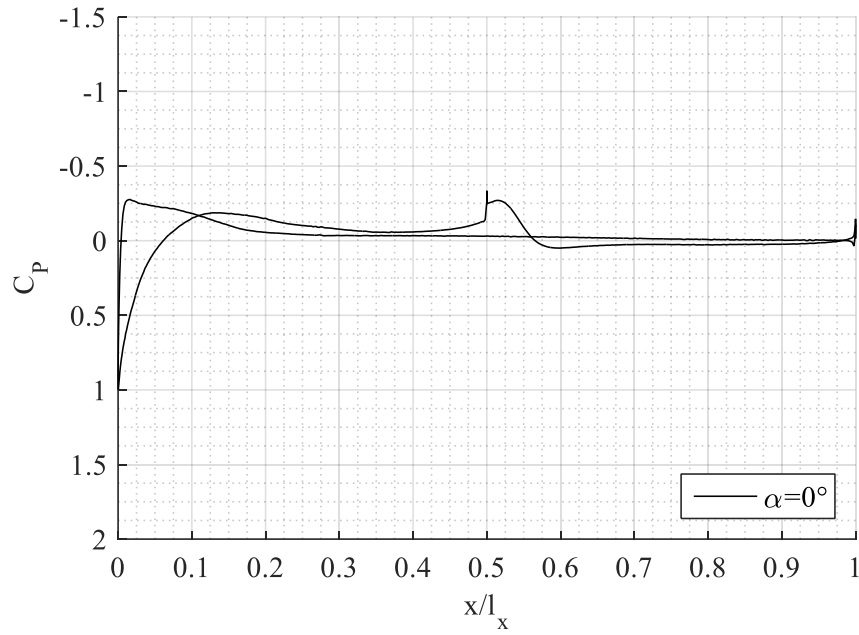


Figure 4.1: Pressure coefficient plot of the base model at 0° angle of attack

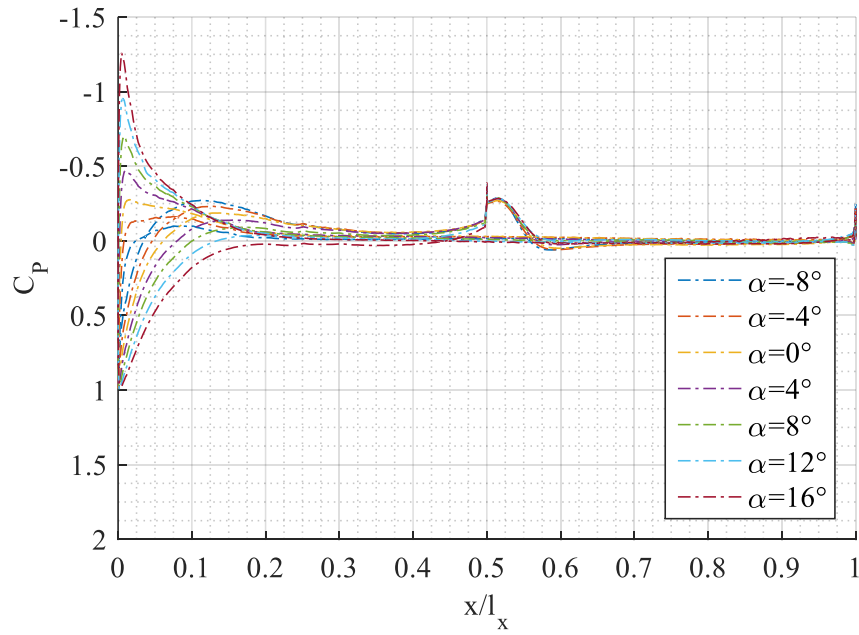


Figure 4.2: Pressure coefficient plot of the base model at various angles of attack

Pressure coefficient plots for cases with varying angles of attack show a continuous distribution on the surface of the fuselage, except at the step region, where the sudden decrease in pressure is observed as expected due to vortices being present at the region.

4.2 Flowfield Analysis

In this section, numerically obtained flow field data comprised of scalar and vector quantities are analyzed for varying flow conditions, and are compared to results obtained with base model (NACA 57-A Hull) at 0° angle of attack.

4.2.1 Dimensionless Wall Distance

Distribution of y^+ contours on fuselage surface is shown below in Figure 4.3, where y^+ is the dimensionless wall distance defined previously in Equation 3.6. From figure, it can be deduced that $y^+_{max} = 1$ is attained throughout the fuselage surface, that is, the height of the first grid cell in contact with the fuselage cavity is low enough to allow the boundary layer to be accurately resolved down to the level of viscous sub layer.

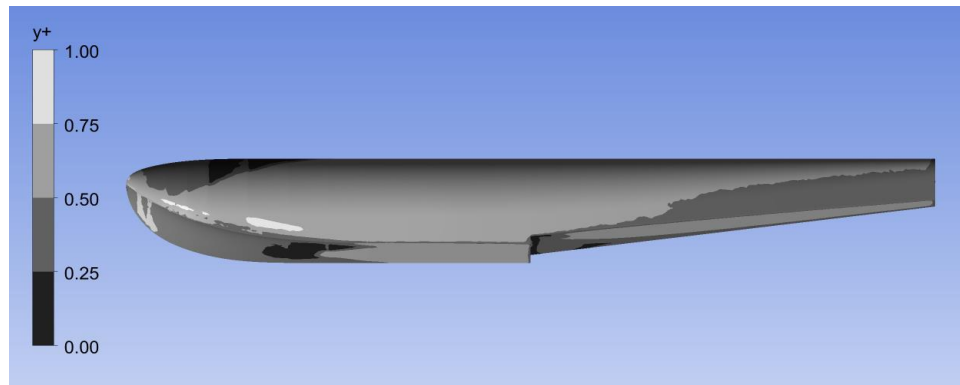


Figure 4.3: y^+ distribution on fuselage surface

4.2.2 Base Model Analysis

Static pressure contours obtained on symmetry plane, fuselage surface and planes normal to the freestream at 0° angle of attack are shown in Figure 4.4, Figure 4.5 and Figure 4.6 below.

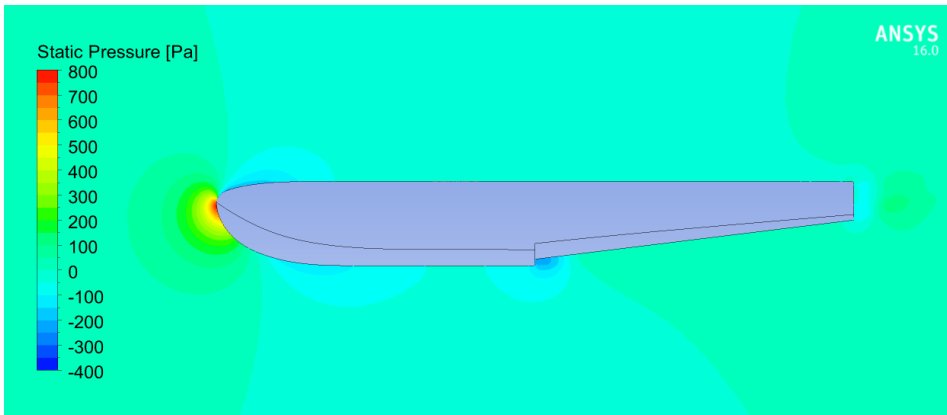


Figure 4.4: Static pressure contours on symmetry plane of NACA Model 57-A hull at 0° angle of attack

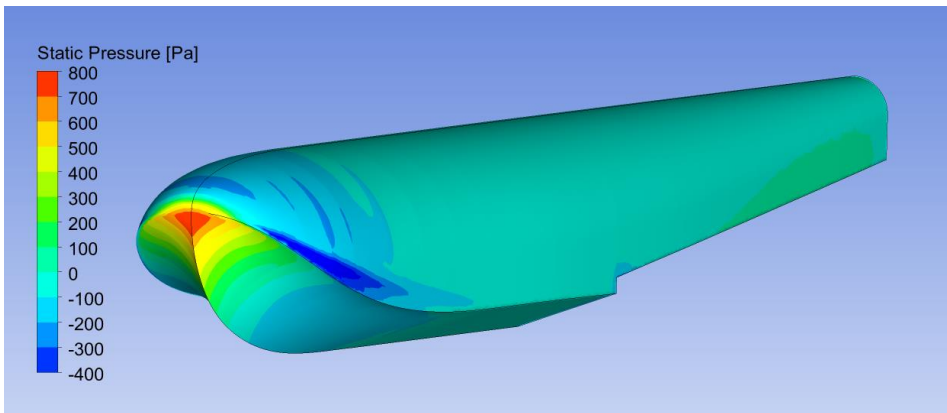


Figure 4.5: Static pressure contours on fuselage surface of NACA Model 57-A hull at 0° angle of attack

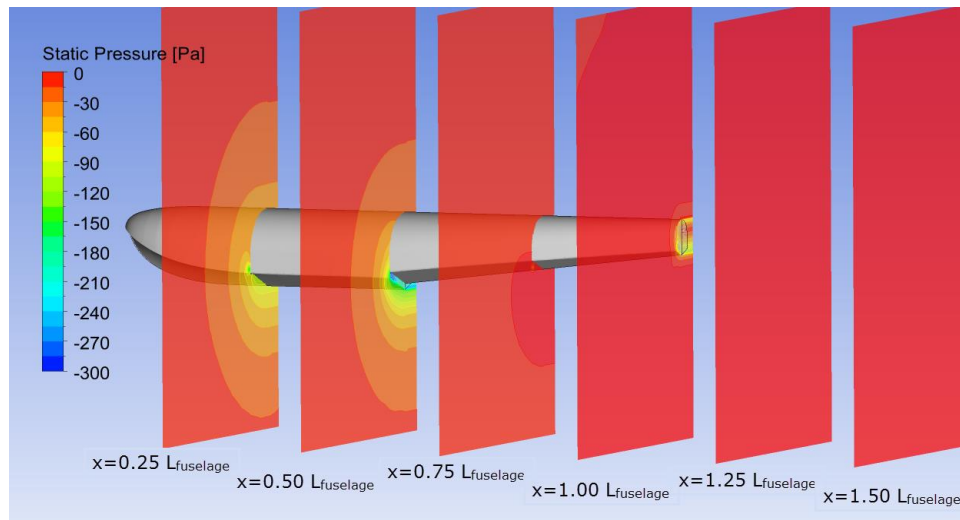


Figure 4.6: Static pressure contours on planes normal to the flow of NACA Model 57-A hull at 0° angle of attack

Streamwise velocity contours on symmetry plane at 0° angle of attack is given in Figure 4.7, and streamlines shown on one half of the body, parted from symmetry plane are given in Figure 4.8 and Figure 4.9 below, respectively.

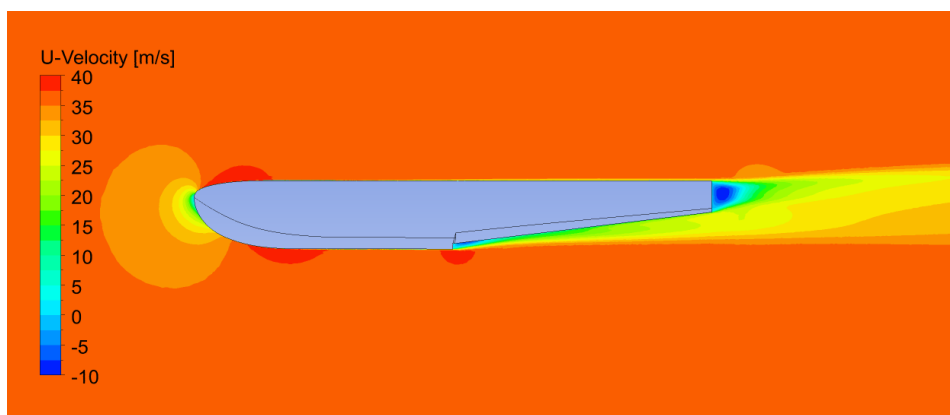


Figure 4.7: Streamwise velocity contours on symmetry plane of NACA Model 57-A hull at 0° angle of attack

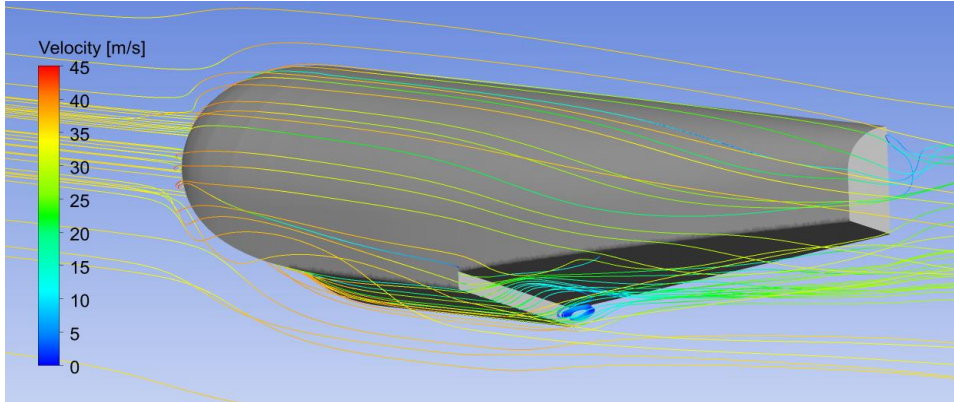


Figure 4.8: Streamlines shown on half-fuselage

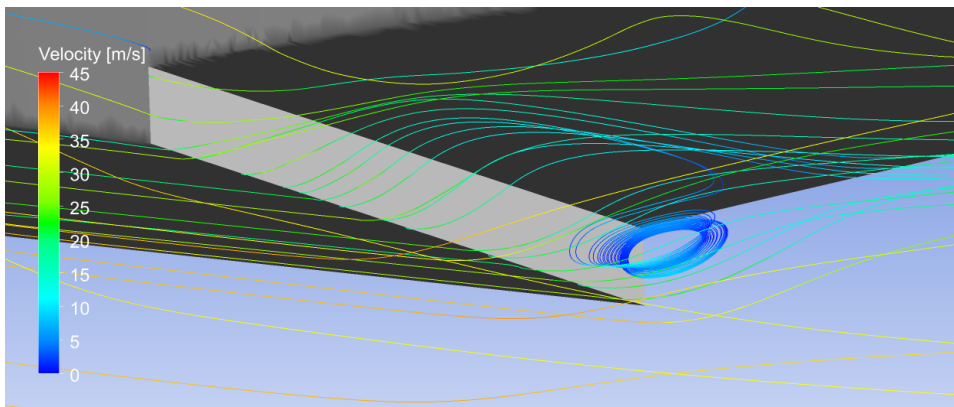


Figure 4.9: Close-up look of streamlines shown on half-fuselage

From above figures, a notable drop in static pressure and negative U-velocities were observed on the step and the wake of the fuselage, as a result of the vortices generated at these regions.

Since flow separation is a significant cause of increase in drag; as an effort to determine the extent of flow separation, thus the size of the vortex-dominated region at the wake of the step, contours of skin friction coefficient in the x-direction were plotted at the surface of the fuselage. Skin friction coefficient is defined with the following relationship:

$$C_f \equiv \frac{\tau_w}{q} \quad (4.1)$$

where τ_w is the wall shear stress, and q is the dynamic pressure defined previously in Equation 2.2. The streamwise component of the skin friction coefficient, C_{fx} , hence the wall shear stress, τ_{wx} was evaluated in plotting the contours, where the change of sign of C_{fx} (inflection points) indicate flow separation points.

Resulting contours of streamwise component of skin friction coefficient is given below in Figure 4.10, where only the contours of negative values of C_{fx} are shown for the purpose of identifying the separated portion of the wall-bounded flow.

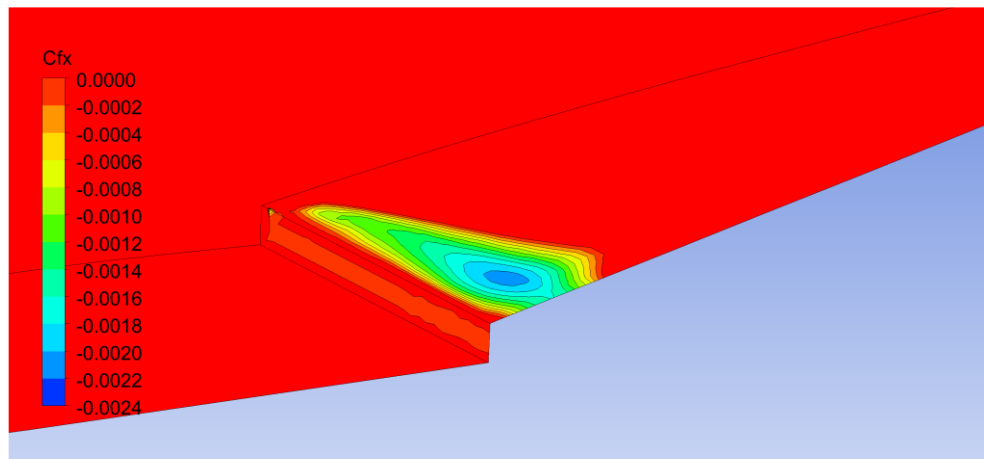


Figure 4.10: Contours of streamwise skin friction coefficient indicating flow separation region at the bottom of the NACA Model 57-A hull at 0° angle of attack

4.2.3 Effect of Angle of Attack

The values of drag coefficient corresponding to the numerical results given in Figure 3.9 are given both in viscous and pressure components and in change percentages with respect to the base model at 0° angle of attack in Table 4.2 and Table 4.3, and the

change in velocity magnitude contours with varying angles of attack is given in Figure 4.11 below.

Table 4.2: Drag breakdowns of varying angles of attack

Angle of Attack	$C_{Dpressure}$	$C_{Dviscous}$
-8°	0.03590	0.02337
-4°	0.02512	0.01963
0°	0.02210	0.02314
4°	0.02680	0.02291
8°	0.04153	0.02246
12°	0.06904	0.02194
16°	0.12420	0.02135

Table 4.3: Drag coefficient results of angles of attack

Angle of Attack	C_D	Percent Change
-8°	0.05927	31.04
-4°	0.04475	-1.06
0°	0.04523	-
4°	0.04971	9.90
8°	0.06400	41.50
12°	0.09099	101.17
16°	0.14555	221.80

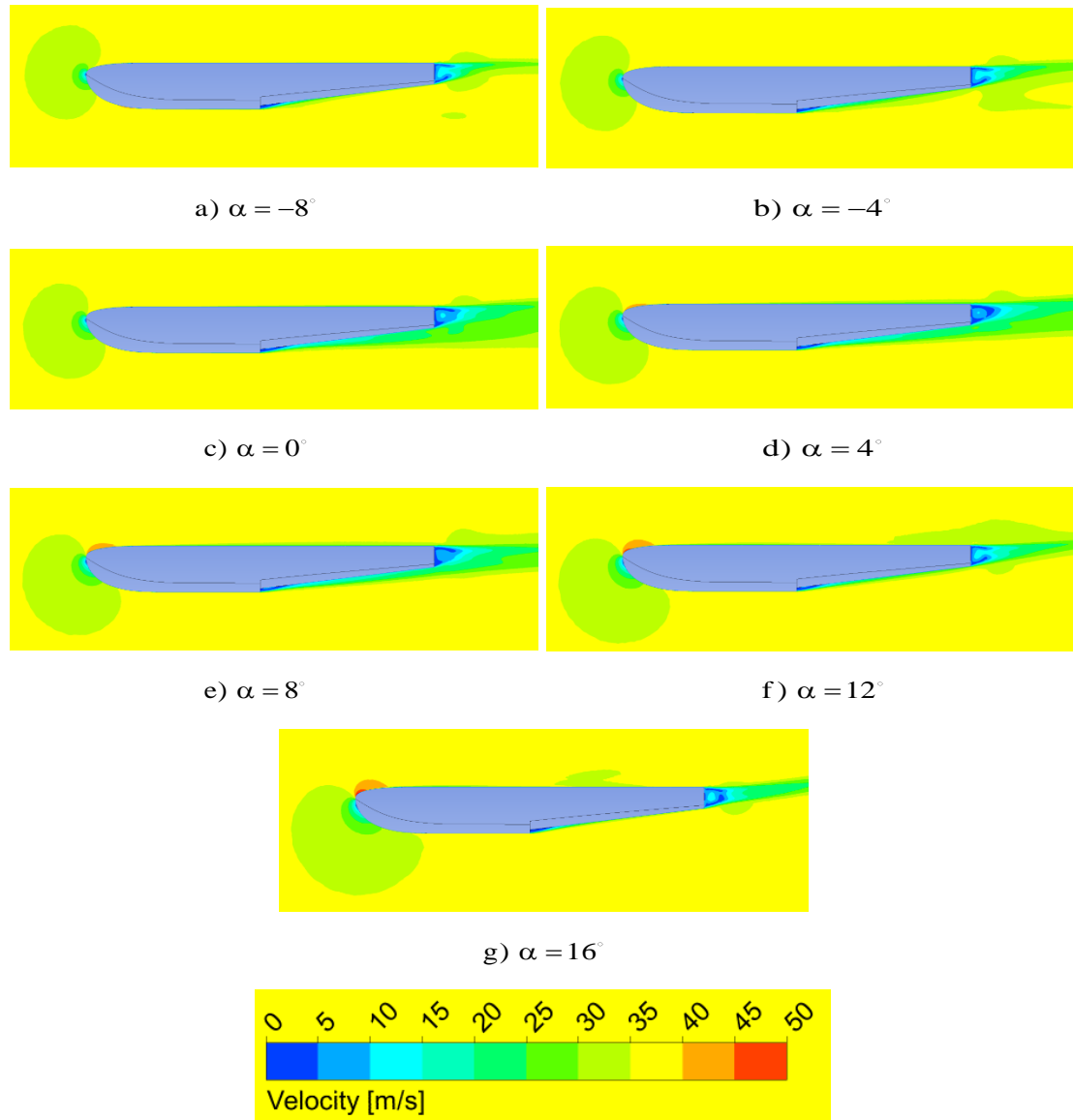


Figure 4.11: Velocity magnitude contours on symmetry plane of NACA Model 57-A hull at various angles of attack

For base model, forward stagnation point and its change with angle of attack, wake regions with local velocity extrema, and regions with velocity vectors in the direction of negative-x due to vortices being present could be seen from Figure 4.11.

4.2.4 Effect of Step Height

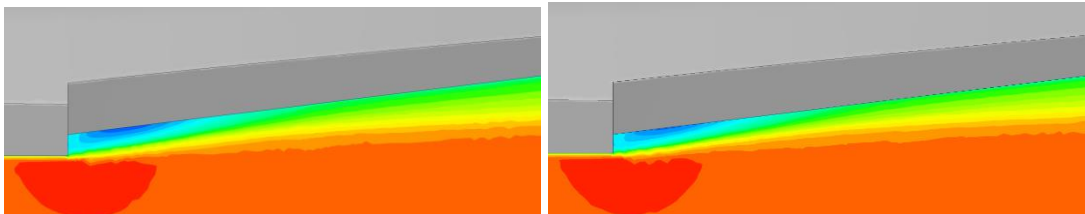
Values of drag coefficient obtained using SST k- ω turbulence model for varying step heights are given as drag breakdowns, and total drag and change percentages from base model in Table 4.4 and Table 4.5, respectively. Streamwise velocity and skin friction coefficient contours are shown in Figure 4.12 and Figure 4.13 below.

Table 4.4: Drag breakdowns of varying step heights

Step Height	$C_{Dpressure}$	$C_{Dviscous}$
0.850 in (0.075 x beam)	0.02210	0.02314
0.741 in (0.065 x beam)	0.02118	0.02315
0.627 in (0.055 x beam)	0.02022	0.02323
0.513 in (0.045 x beam)	0.01972	0.02335

Table 4.5: Drag coefficient results of varying step heights

Step Height	C_D	Percent Change
0.850 in (0.075 x beam)	0.04523	-
0.741 in (0.065 x beam)	0.04433	-2.01
0.627 in (0.055 x beam)	0.04345	-3.95
0.513 in (0.045 x beam)	0.04307	-4.79



a) Step Height = 0.075b

b) Step Height = 0.065b

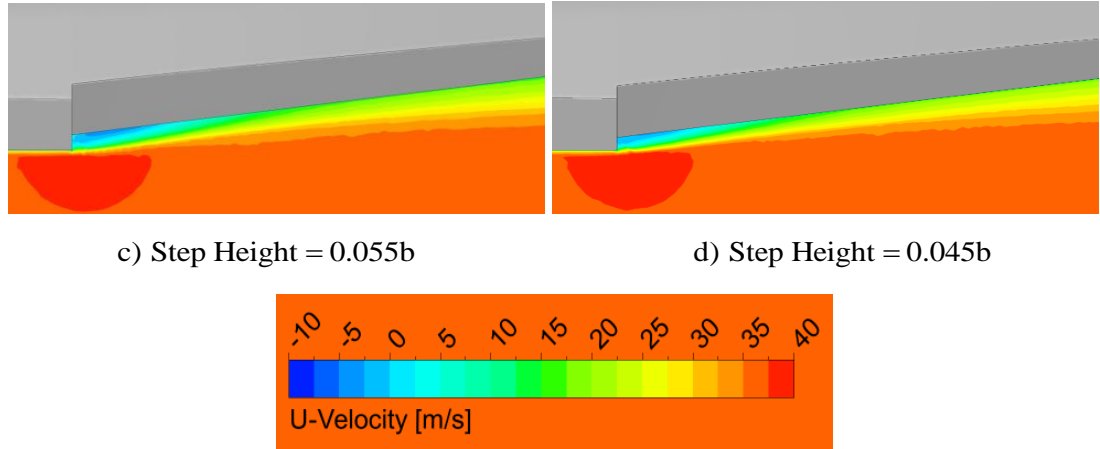


Figure 4.12: Streamwise velocity contours for cases with varying step heights

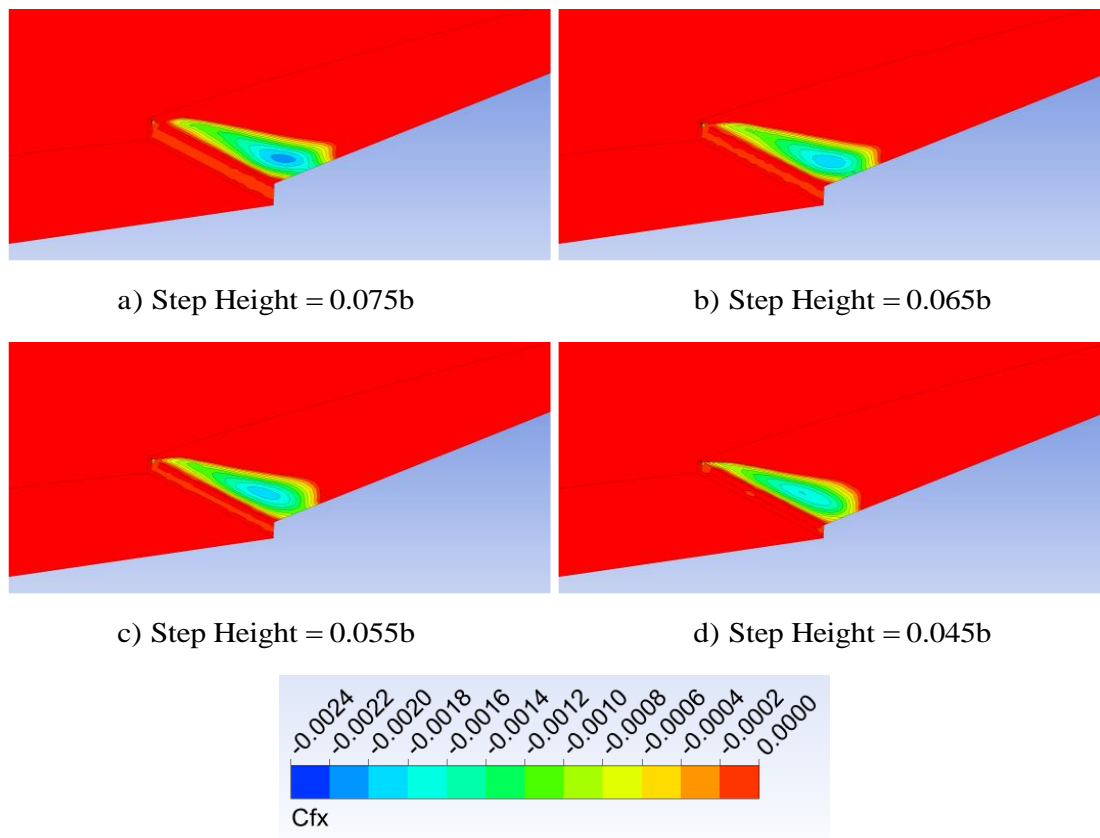


Figure 4.13: Streamwise skin friction coefficient contours for cases with varying step heights

From Table 4.4, Table 4.5, Figure 4.12 and Figure 4.13, it could be seen that the drag coefficient is decreasing with a decrease in step height, up to 4.79% from the base model. As the change in the parameter affected the pressure drag prominently, it had limited effect on the viscous drag of the fuselage. It was also seen that the vortex region got smaller in size gradually with each decrease in step height.

4.2.5 Effect of Sternpost Angle

Change in drag of the fuselage with respect to the change in sternpost angle was investigated, and the resulting drag breakdowns, drag coefficient results, streamwise velocity and skin friction coefficient contours for varying sternpost angles are given below in Table 4.6, Table 4.7, Figure 4.14 and Figure 4.15, respectively.

Table 4.6: Drag breakdowns of varying sternpost angles

Sternpost Angle	$C_{D_{\text{pressure}}}$	$C_{D_{\text{viscous}}}$
7°	0.02210	0.02314
8°	0.02209	0.02321
9°	0.02249	0.02323

Table 4.7: Drag coefficient results of varying sternpost angles

Sternpost Angle	C_D	Percent Change
7°	0.04523	-
8°	0.04531	0.16
9°	0.04571	1.06

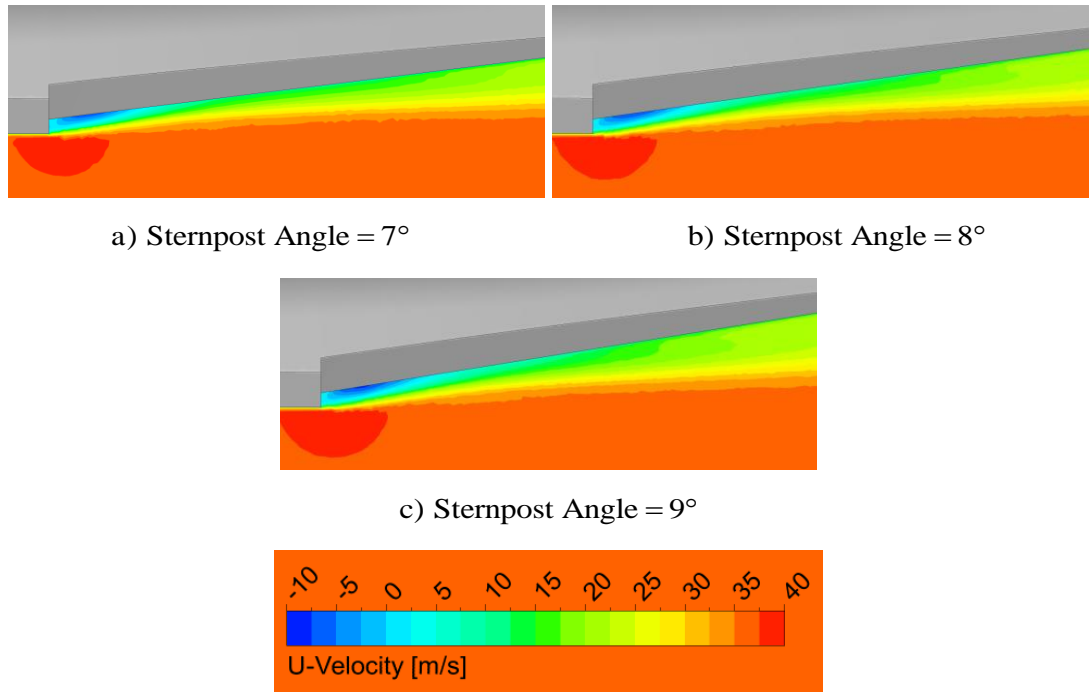
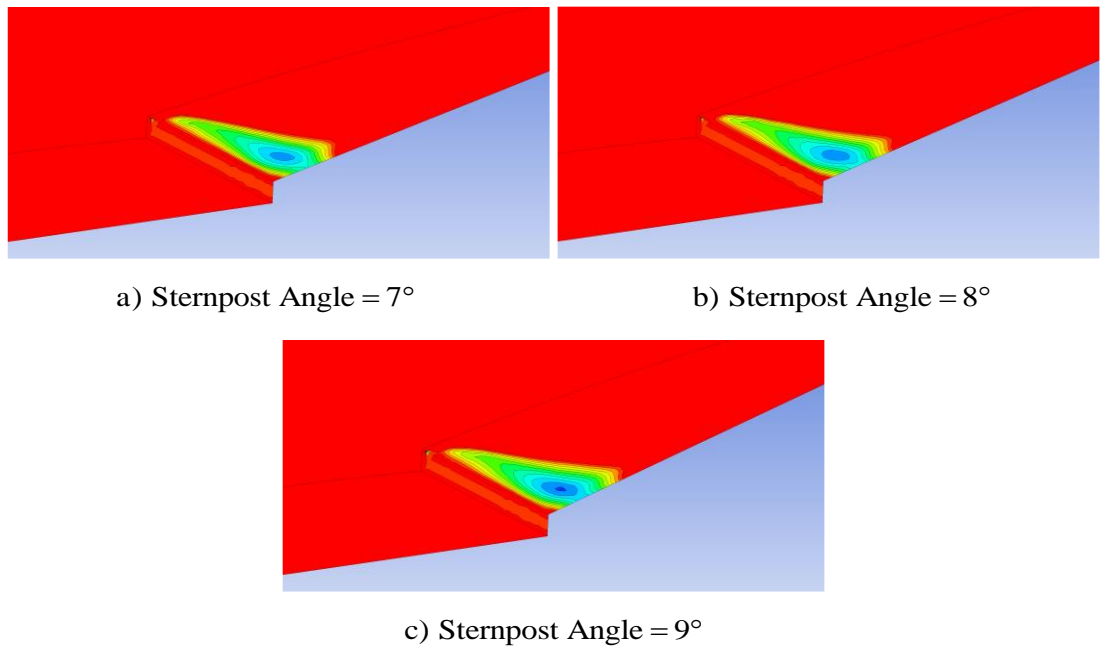


Figure 4.14: Streamwise velocity contours for cases with varying sternpost angles



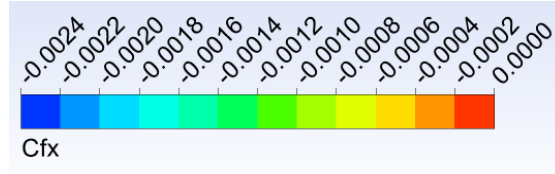


Figure 4.15: Streamwise skin friction coefficient contours for cases with varying sternpost angles

The increase in sternpost angle resulted in an increase in drag of the fuselage as well up to 1.06% from the base model, with the lower velocity region (compared to freestream velocity) at the wake of the step slightly expanding in size, as shown in Figure 4.14. While the change of the parameter from 7° to 8° had little effect on the drag of the body, it was seen that the pressure drag increased with the increase of sternpost angle to 9°.

4.2.6 Effect of Deadrise Angle

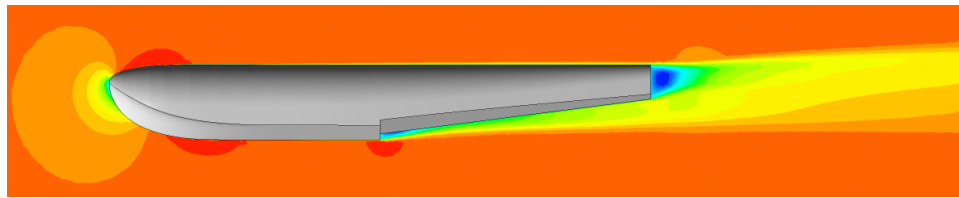
The effect of varying deadrise angle on the drag of the fuselage is shown in Table 4.8 and Table 4.9, and the streamwise velocity and skin friction coefficient contours are shown in Figure 4.16 and Figure 4.17 below.

Table 4.8: Drag breakdowns of varying deadrise angles

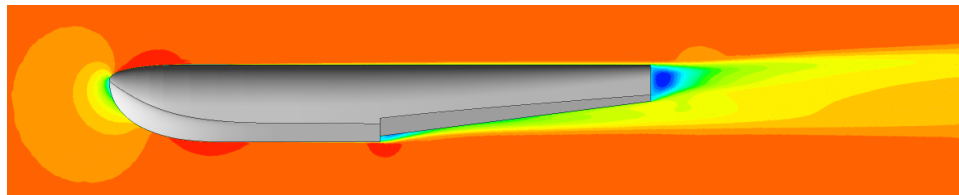
Deadrise Angle	$C_{Dpressure}$	$C_{Dviscous}$
20°	0.02210	0.02314
25°	0.02289	0.02340
30°	0.02489	0.02327

Table 4.9: Drag coefficient results of varying deadrise angles

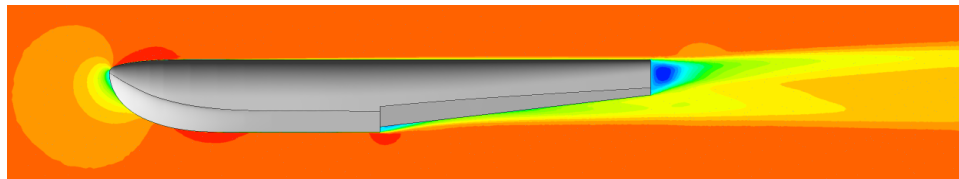
Deadrise Angle	C_D	Percent Change
20°	0.04523	-
25°	0.04629	2.32
30°	0.04817	6.48



a) Deadrise Angle = 20°



b) Deadrise Angle = 25°



c) Deadrise Angle = 30°

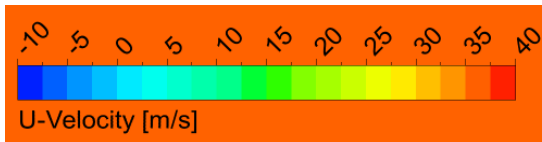


Figure 4.16: Streamwise velocity contours for cases with varying deadrise angles

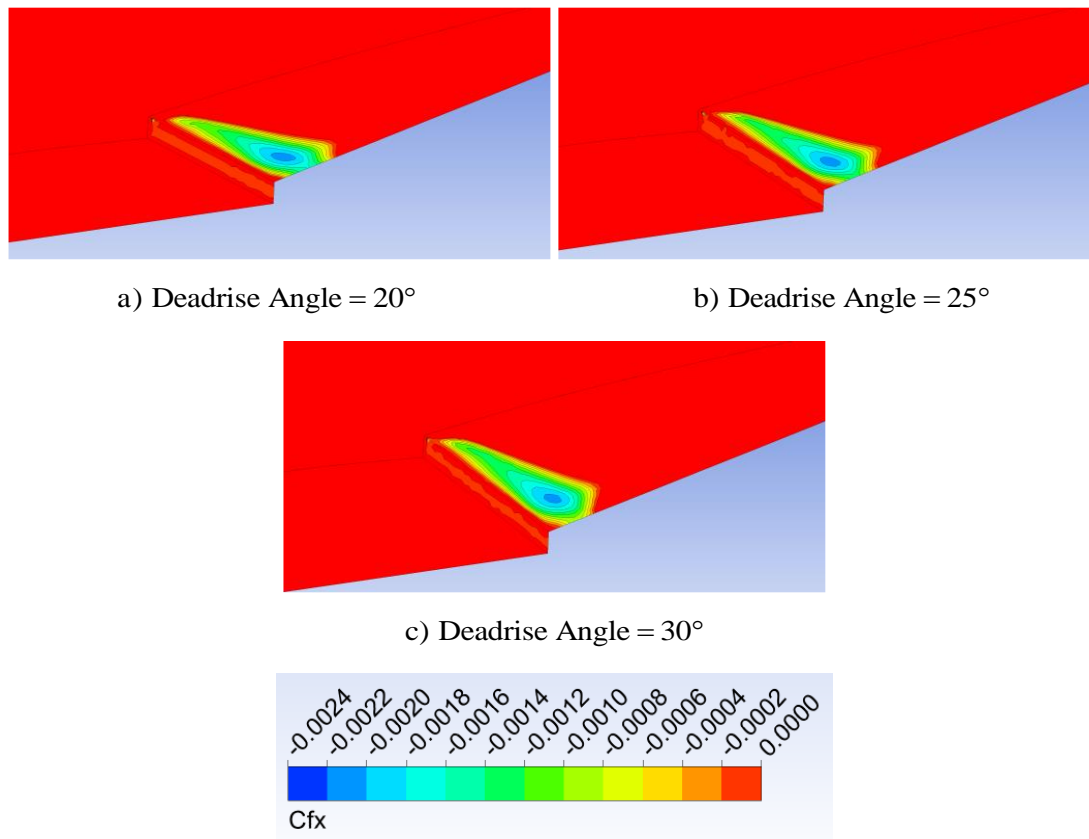


Figure 4.17: Streamwise skin friction coefficient contours for cases with varying deadrise angles

Similar to the effect of sternpost angle, it could be seen that the drag coefficient is increasing up to 6.48% with the increase in deadrise angle, again mostly due to increase in pressure drag, while the parameter is in the region of hydrodynamic requirement limits.

4.2.7 Effect of Parameters on Volume of the Fuselage

Since volume of the fuselage is another important design variable, change in volume of the fuselage with respect to change in fuselage parameters are calculated. Resulting values of volume and difference percentages from base model are given in Table 4.10.

Table 4.10: Change in fuselage volume with respect to varying fuselage parameters

Fuselage Parameter	Fuselage Volume	Percent Change
Step Height		
0.850 in	5,935.60 in ³	-
0.741 in	5,972.94 in ³	0.63
0.627 in	6,012.00 in ³	1.29
0.513 in	6,050.58 in ³	1.94
Sternpost Angle		
7°	5,935.60 in ³	-
8°	5,828.33 in ³	-1.81
9°	5,719.88 in ³	-3.63
Deadrise Angle		
20°	5,935.60 in ³	-
25°	5,947.74 in ³	0.20
30°	5,959.07 in ³	0.40

From Table 4.10, it was seen that the increase in sternpost angle is relatively having the most effect on fuselage volume, a reduction of up to 3.63%; while the increase in deadrise angle is only affecting the volume up to 0.4%.

4.2.8 Combined Effect of Step Height and Sternpost Angle

Sternpost angle varying between 7° and 9° and the step height varying between 4% and 8% of the beam length have been further investigated together to better understand the effect that the vortices have on aerodynamic drag, which are occurring at the step region and extending to a portion of sternpost. Since it was seen that the deadrise angle does not have a direct effect on the vortices occurring at the bottom of the fuselage, only the combined effect of step height and the sternpost angle affecting the region was investigated. Resulting drag coefficient values and their comparison to the base model

are given in Table 4.11 and Table 4.12, and the change in volume of the fuselage with respect to change in fuselage parameters is given in Table 4.13 and Table 4.14.

Table 4.11: Values of drag coefficient obtained with varying step heights and sternpost angles

C _D Step Height	Sternpost Angle		
	7°	8°	9°
0.513 in (0.045 x beam)	0.04307	0.04271	0.04236
0.627 in (0.055 x beam)	0.04345	0.04320	0.04293
0.741 in (0.065 x beam)	0.04433	0.04420	0.04390
0.850 in (0.075 x beam)	0.04523	0.04531	0.04571

Table 4.12: Percent change of drag coefficient obtained with varying step heights and sternpost angles from the base model

Percent Change Step Height	Sternpost Angle		
	7°	8°	9°
0.513 in (0.045 x beam)	-4.79	-5.57	-6.36
0.627 in (0.055 x beam)	-3.95	-4.50	-5.10
0.741 in (0.065 x beam)	-2.01	-2.30	-2.95
0.850 in (0.075 x beam)	-	0.16	1.06

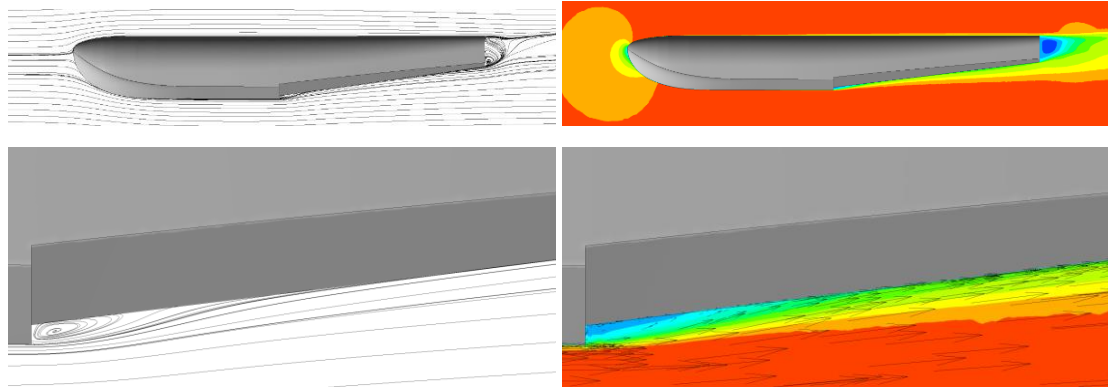
Table 4.13: Change in fuselage volume with respect to varying step heights and sternpost angles

Fuselage Volume (in ³) Step Height	Sternpost Angle		
	7°	8°	9°
0.513 in (0.045 x beam)	6,050.58	5,943.77	5,835.33
0.627 in (0.055 x beam)	6,012.00	5,904.72	5,796.28
0.741 in (0.065 x beam)	5,972.94	5,865.67	5,757.22
0.850 in (0.075 x beam)	5,935.60	5,828.33	5,719.88

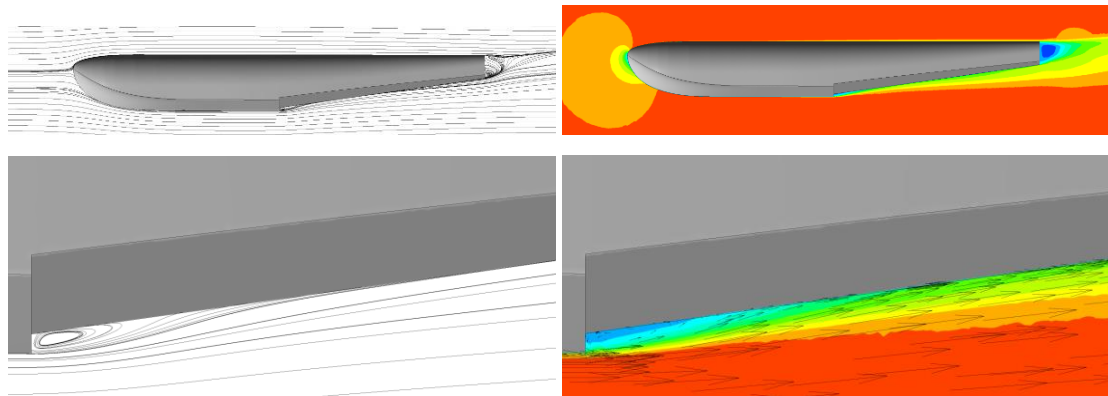
Table 4.14: Percent change in fuselage volume with respect to varying step heights and sternpost angles

Percent Change Step Height	Sternpost Angle		
	7°	8°	9°
0.513 in (0.045 x beam)	1.94	0.14	-1.69
0.627 in (0.055 x beam)	1.29	-0.52	-2.35
0.741 in (0.065 x beam)	0.63	-1.18	-3.01
0.850 in (0.075 x beam)	-	-1.81	-3.63

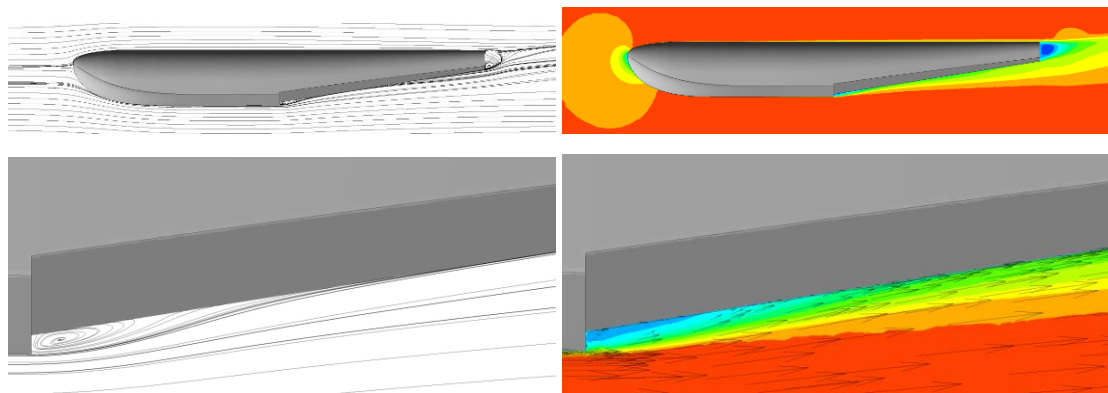
Resulting streamlines and streamwise velocity contours for varying step heights and sternpost angles are given in Figure 4.18 to Figure 4.21.



a) Sternpost Angle = 7°

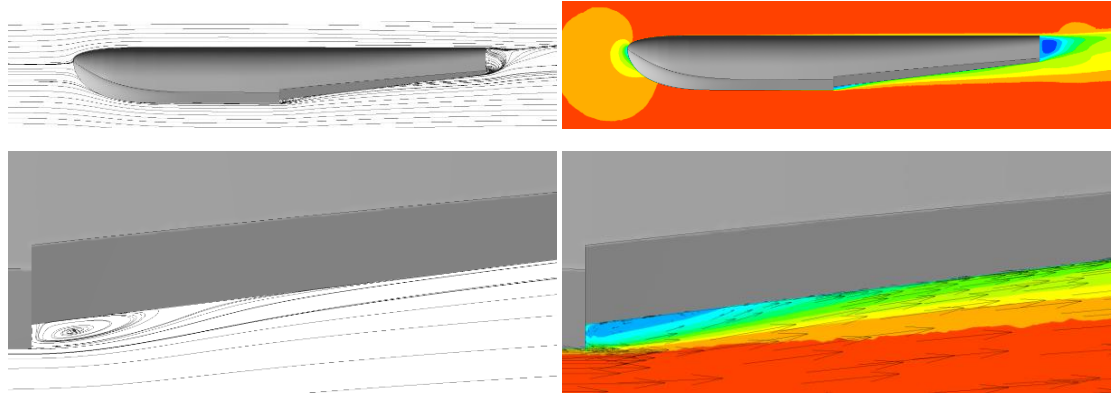


b) Sternpost Angle = 8°

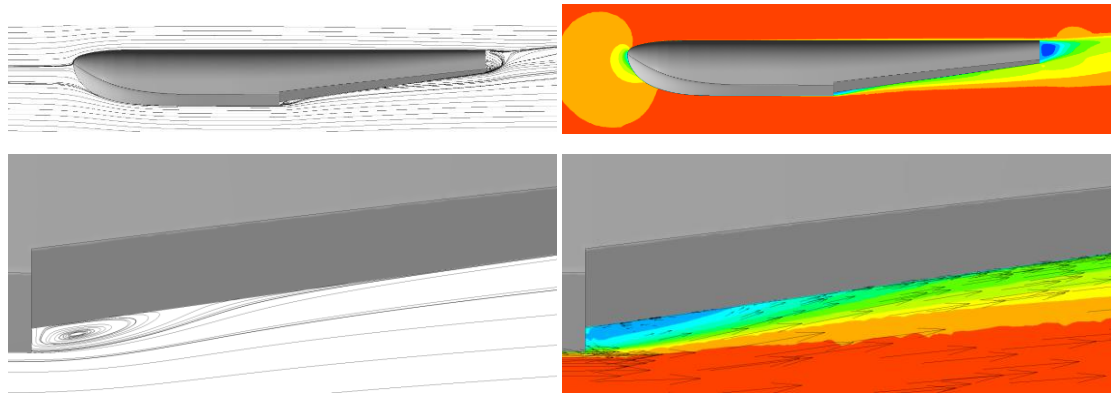


c) Sternpost Angle = 9°

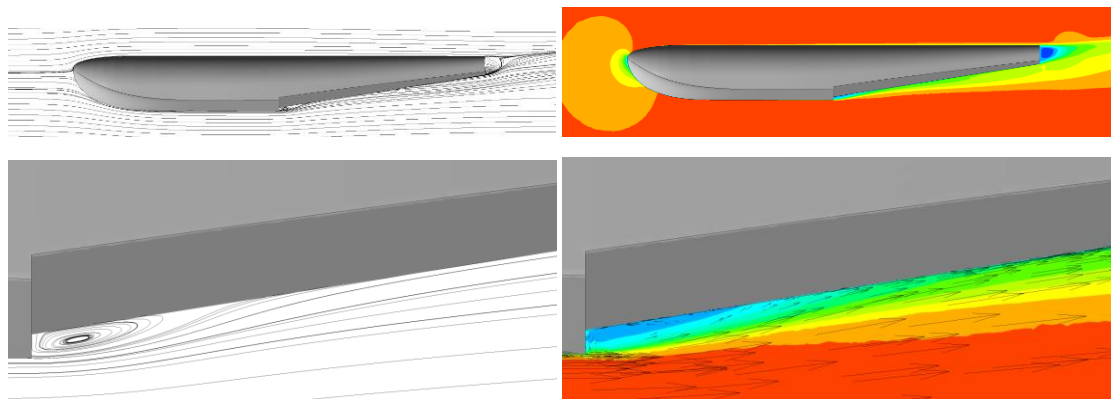
Figure 4.18: Streamlines and streamwise velocity contours for the case with 0.513 in step height and varying sternpost angle



a) Sternpost Angle = 7°

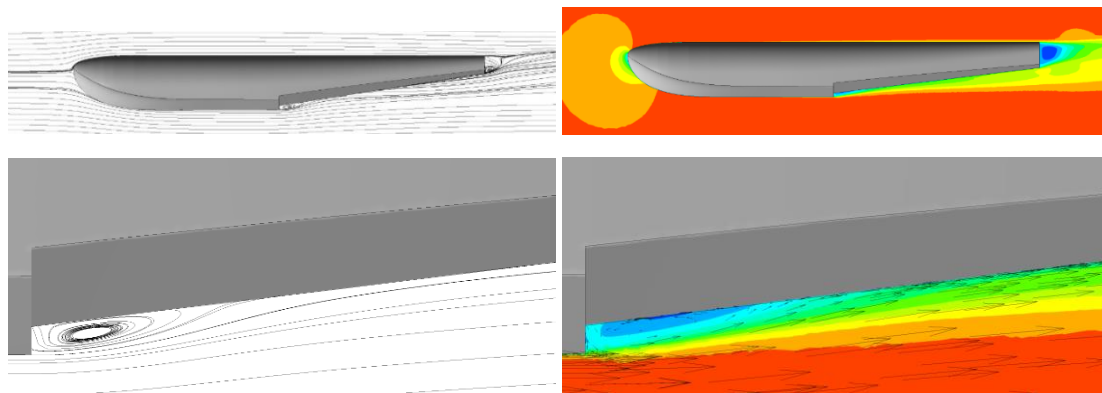


b) Sternpost Angle = 8°

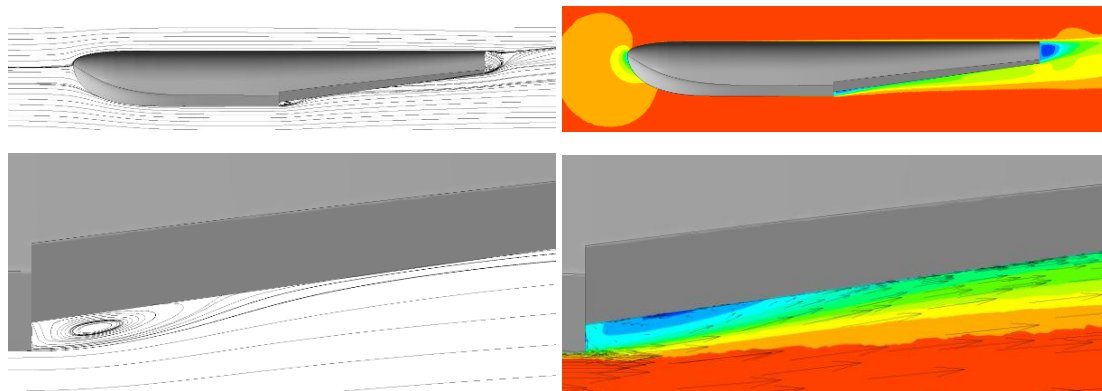


c) Sternpost Angle = 9°

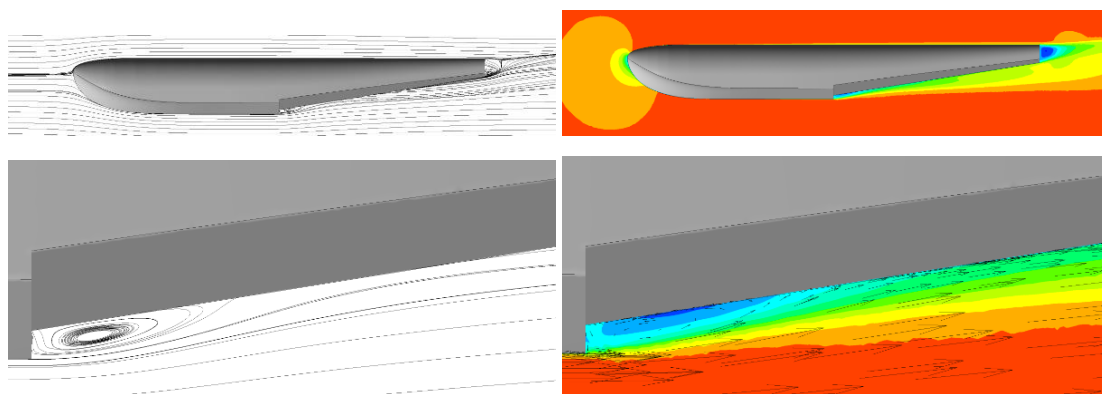
Figure 4.19: Streamlines and streamwise velocity contours for the case with 0.627 in step height and varying sternpost angle



a) Sternpost Angle = 7°

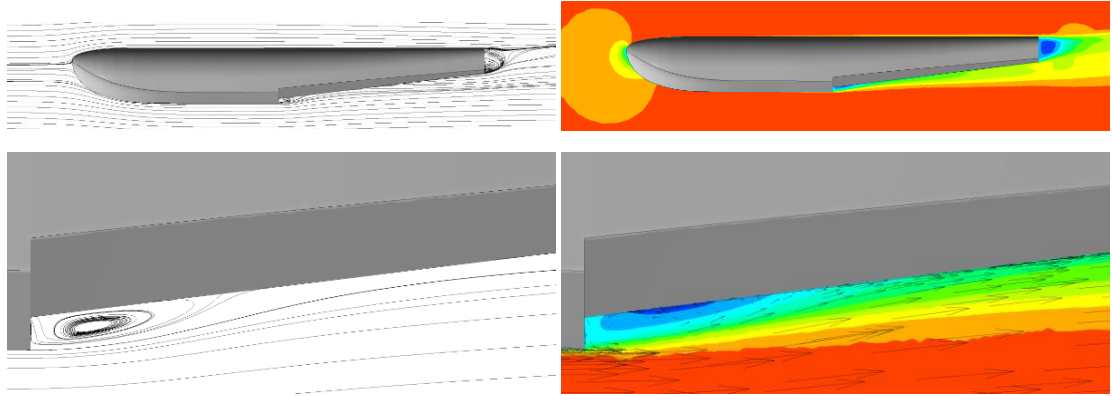


b) Sternpost Angle = 8°

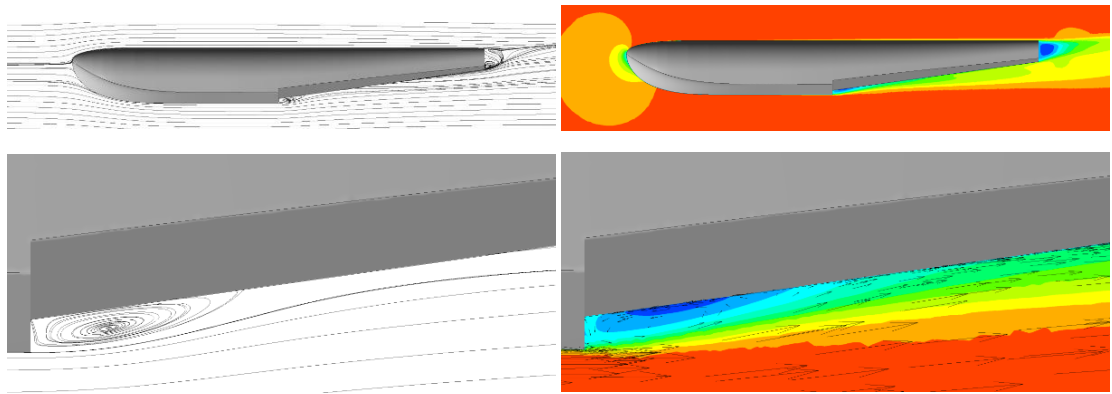


c) Sternpost Angle = 9°

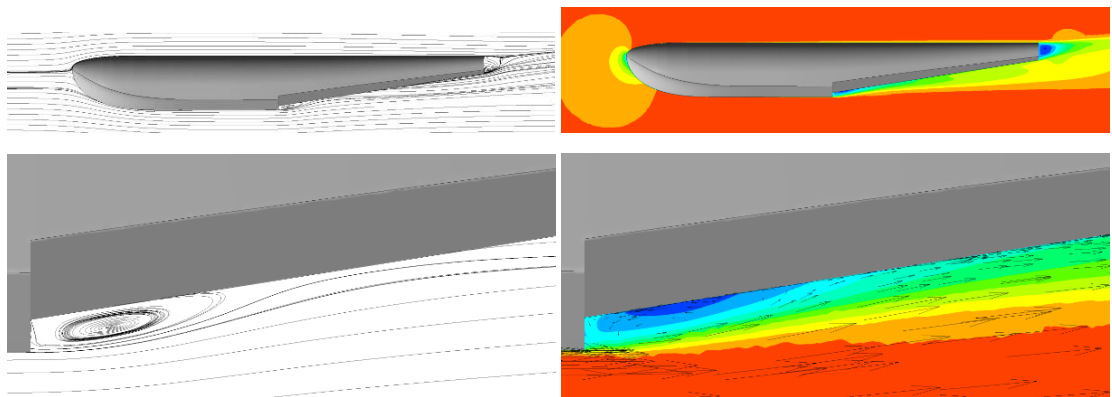
Figure 4.20: Streamlines and streamwise velocity contours for the case with 0.741 in step height and varying sternpost angle



a) Sternpost Angle = 7°



b) Sternpost Angle = 8°



c) Sternpost Angle = 9°

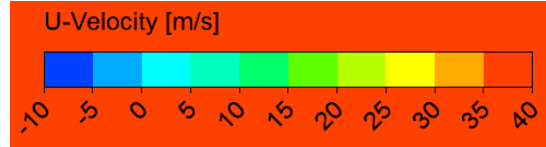


Figure 4.21: Streamlines and streamwise velocity contours for the case with 0.850 in step height and varying sternpost angle

From Table 4.11 to Table 4.14, and from Figure 4.18 to Figure 4.21, it was seen that unlike the base model, as the step height is reduced, an increase in sternpost angle is reducing the drag coefficient, due to the fact that the vortex region in the wake of the fuselage are getting smaller in the process although the vortex region in the step is getting larger in size, which makes the two properties acting opposite on the drag of the fuselage. There is a 7.42% difference for the cases where sternpost angle is held constant as 9° and the step height is changed between 4.5% and 7.5% of the beam length, therefore it could be stated that with the increase in sternpost angle, change in step height is having a greater effect on the drag of the fuselage.

4.3 Ground Effect

A parametric ground effect study has been conducted to investigate the ground effect that resembles to that of take-off and landing conditions at water, on the vortex regions at the bottom of the wall and ultimately on the fuselage drag of the base model. The distance of the fuselage bottom from the bottom face of the computational domain has been varied from 0.1 to 1.0 of the fuselage length (with $L_{fuselage}=84.00$ inches or 2.13 meters), and the boundary condition of the bottom face has been changed to no-slip moving wall, with the velocity being equal to freestream velocity of 35.78 m/s. The resulting trend of drag coefficient is given in the plot below in Figure 4.22.

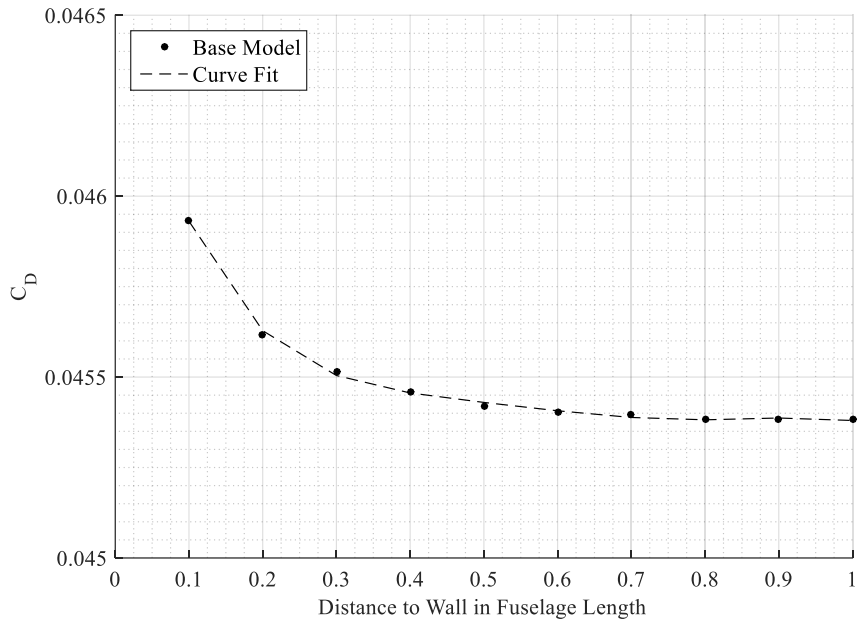


Figure 4.22: Drag coefficient trend of varying distances between the bottom of the fuselage and the bottom wall of the domain at 0° angle of attack

4.4 Reynolds Number Effect

The effect of Reynolds Number on drag of the fuselage has also been studied to investigate the magnitude of the effect on aerodynamic drag. Dimensionless wall distance $y^+_{max} \approx 1$ has been held constant on fuselage surface with each case with varying Reynolds Number by changing the wall adjacent cell height of the grid accordingly. The resulting values of wall adjacent cell height are given in Table 4.15. Drag coefficients are given in Table 4.16 and Table 4.17, and shown in Figure 4.23 in comparison.

Table 4.15: Wall adjacent cell heights of grids for cases with varying Reynolds Numbers

Reynolds Number	Δy
1.30×10^6	0.03916 mm
2.60×10^6	0.02058 mm
5.20×10^6	0.01108 mm
1.04×10^7	0.00568 mm
2.08×10^7	0.00298 mm

Table 4.16: Drag breakdowns of varying Reynolds Numbers

Reynolds Number	$C_{D\text{pressure}}$	$C_{D\text{viscous}}$
1.30×10^6	0.02209	0.01680
2.60×10^6	0.02226	0.02059
5.20×10^6	0.02210	0.02314
1.04×10^7	0.02253	0.02210
2.08×10^7	0.02306	0.02038

Table 4.17: Effect of Reynolds Number on drag of the base model

Reynolds Number	C_D	Percent Change
1.30×10^6	0.03889	-14.02
2.60×10^6	0.04285	-5.27
5.20×10^6	0.04523	-
1.04×10^7	0.04463	-1.33
2.08×10^7	0.04345	-3.96

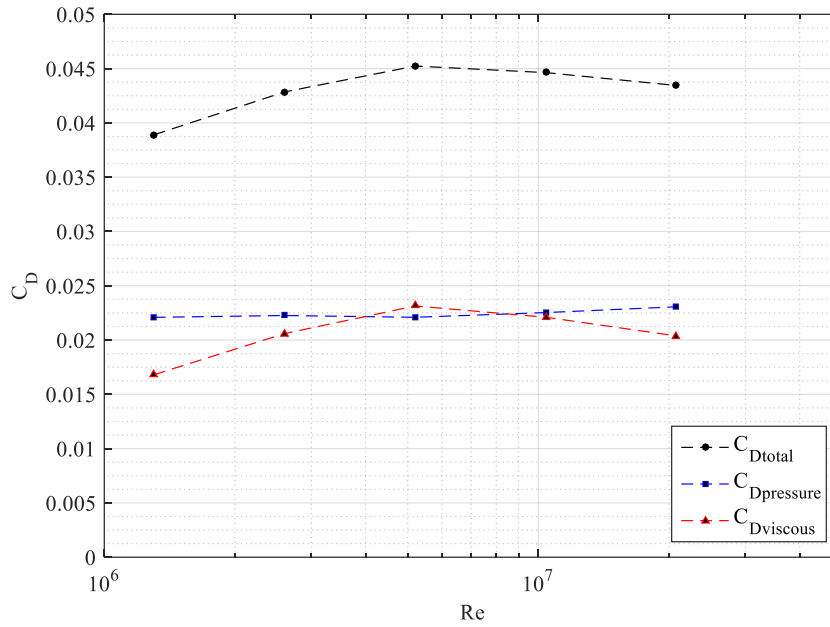


Figure 4.23: Drag coefficient trend of varying flow Reynolds Numbers

From Table 4.17 and Figure 4.23, it can be seen that the drag coefficient of the body is increasing with respect to the increase in flow Reynolds Number up until $Re = 5.20 \times 10^6$, at which point forward a slight reduction is observed. From Table 4.16, it was also observed that the viscous drag is the primary component that affects the change in total drag of the body, whereas pressure drag remains almost constant. Contours of turbulence intensity have been plotted to investigate the effect, where turbulence intensity is defined as:

$$Tu = \frac{u'}{U} \quad (4.1)$$

Here, u' is the root-mean-square of the fluctuating components of velocity and U is the mean velocity component. Resulting turbulence intensity contours are given below in Figure 4.24.

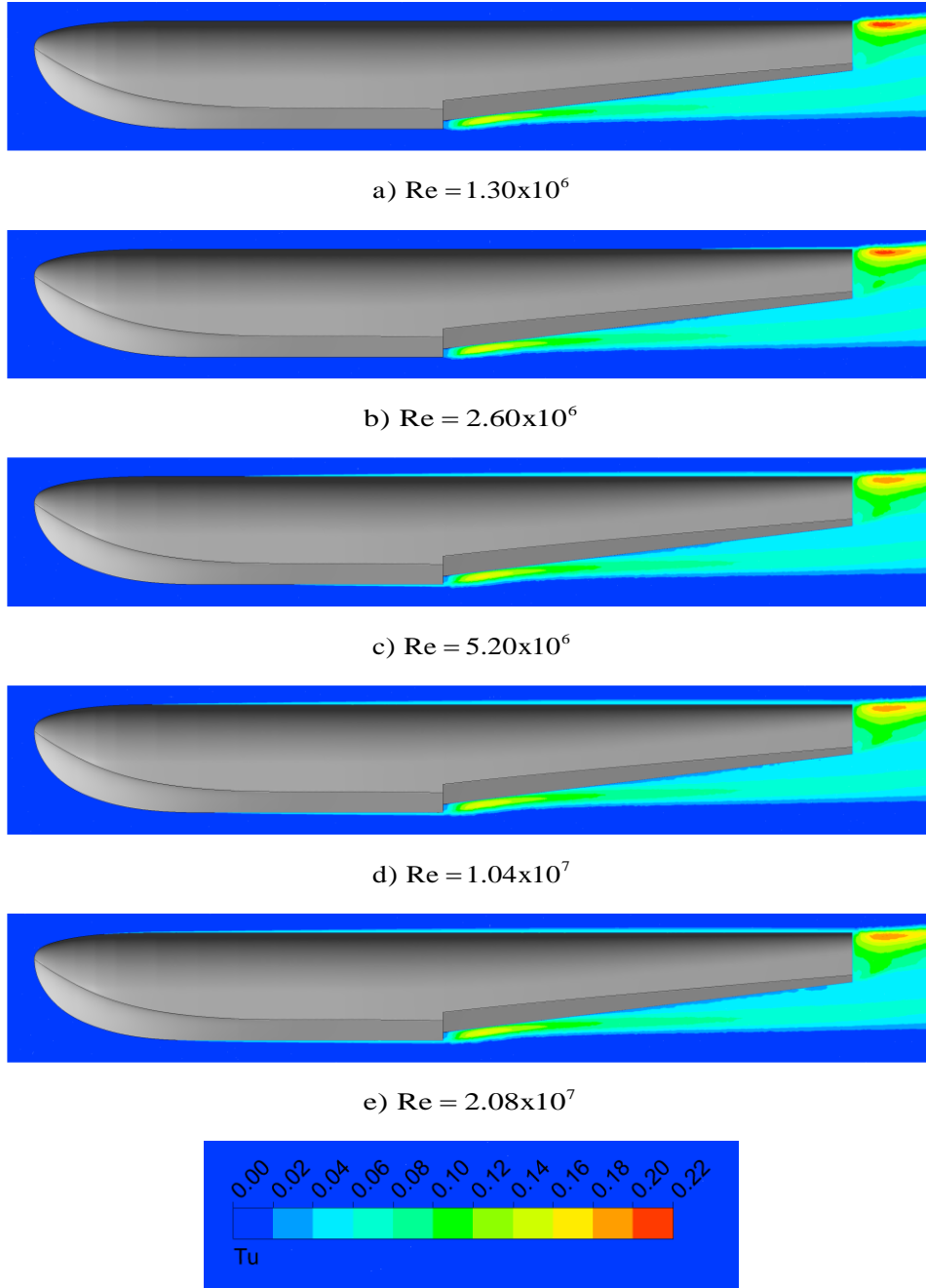


Figure 4.24: Turbulence intensity contours shown on symmetry plane for cases with varying Reynolds Numbers

From Figure 4.24, it was observed that in the case with $Re=1.30 \times 10^6$, which is the case with the lowest values of drag coefficient attained, flow regime of boundary layer at both the upper surface and the forward lower surface of the fuselage is laminar.

As the flow Reynolds Number is doubled to $Re=2.60 \times 10^6$, a transitional regime first occurs to the aft of the upper surface of the fuselage, with a laminar boundary layer still attained at the lower surface. At $Re=5.20 \times 10^6$, transition point at upper surface of the fuselage moves forward to the bow, and a transitional regime is observed at the lower surface as well.

As a result of further increasing flow Reynolds Number to first $Re=1.04 \times 10^7$ and then to $Re=2.08 \times 10^7$, transition points at both the upper and the lower surface of the fuselage moves further to the bow, finally resulting in a fully turbulent boundary layer through most of the fuselage surface, and in turn in a slight decrease in drag coefficient.

CHAPTER 5

CONCLUSION AND FUTURE WORK

Effects of several geometric parameters on aerodynamic drag of the fuselage, along with the comparison of numerical and experimental data were evaluated in the study. The difference between the numerical and experimental results were, to some extent due to computational models of the hull shaped fuselages being generated by the extrapolation of available cross-sectional dimensions, hence slightly differing in shape from the models in respective studies.

The flow is strongly influenced by separation and eddies at the wake and the step regions regardless of the angle of attack, as seen in Figure 4.4 to Figure 4.10; and results obtained with SST $k-\omega$ turbulence model, which is widely used for problems with such flows agrees well with the experimental data. Pressure coefficient plot shows a smooth distribution along the surface of the fuselage, and a discontinuity right at the step region as expected.

Table 4.5 shows that within hydrodynamic performance constraints, reducing step height results in a decrease in cruise drag as much as 4.79%. It was also observed that the separated region of flow got gradually smaller in size, which is considered as the primary reason for the decrease in pressure drag. While change in sternpost angle from 7° to 8° does not affect drag coefficient significantly, the change in this parameter from 8° to 9° results in an increase of 1.06%, given in Table 4.7. The increase in angle also resulted the separated flow region to grow slightly. Table 4.9 shows that an increase in deadrise angle from 20° to 30° also increases drag coefficient by 6.48%, which makes this parameter relatively having the greatest effect on the drag of the fuselage. An effect similar in magnitude, though resulting in a decrease in drag coefficient opposed to an increase, is obtained in the combined case where the step height is reduced to the 4.5%

of the beam length and the sternpost angle is increased to 9° , lowest and highest values, respectively, in the suggested limits of the parameters. This resulted in a decrease in drag coefficient up to 6.36% of the drag of the base model.

Ground effect study has shown that despite the drag of the fuselage slightly increases as the distance of the fuselage bottom to the moving no-slip wall located at the bottom of the computational domain decreases, as the trend shows in Figure 4.22; it does not affect the drag of the body significantly. A significant ground effect is expected in case of the complete aircraft body along with lifting surfaces is exposed to the similar effect, resulting in a decrease in lift-induced drag and in turn, an increase in lift-to-drag ratio of the aircraft.

It was seen that decreasing flow Reynolds Number to one-fourth (from 5.20×10^6 to 1.30×10^6) also results in a decrease of 14.02% in drag coefficient as a consequence of attaining a laminar boundary layer through the upper surface and the forward lower surface. As the Reynolds Number doubled twice to 1.04×10^7 and 2.08×10^7 , a decrease in drag coefficient was observed up to 3.96% as a result of the fully turbulent boundary layer observed through most of the fuselage.

It can be concluded that as well as flow conditions, fuselage parameters indeed can have a considerable effect on the drag of the fuselage and in turn, in the drag of the aircraft, due to presence of vortices in the discontinuities of geometry for hydrodynamic requirements.

As future work, the following could be considered:

- Investigation of multiple stepped hulls, step fairings and hull bottom shapes and their effects on aerodynamic drag
- Validation of aerodynamic drag of changing fuselage parameters and flow conditions with wind tunnel experiments

REFERENCES

- [1] Parkinson, J. B., Olson, R. E. and House, R. O., “Hydrodynamic and Aerodynamic Tests of a Family of Models of Seaplane Floats with Varying Angles of Dead Rise”, Technical Note No. 716, NACA, 1939.
- [2] Odedra, J., Hope, G. and Kennell, C. “Use of Seaplanes and Integration within a Sea Base”, Technical Report No. NSWCCD-20-TR-2004/08, NSWCCD (Naval Surface Warfare Center Carderock Division), 2004.
- [3] Eubank, R. D., “Autonomous Flight, Fault, and Energy Management of the Flying Fish Solar-Powered Seaplane”, University of Michigan, 2012.
- [4] Canamar, A. L., “Seaplane Conceptual Design and Sizing”, University of Glasgow, 2012.
- [5] Nicolaou, S., *Flying Boats and Seaplanes: A History from 1905*, MBI Publishing, 1998.
- [6] Petrescu, R. V. and Petrescu, F. I., *The Aviation History*, Books on Demand, 2013.
- [7] Barrie Aircraft Museum, De Havilland Canada DHC-3 Otter, Online image, Retrieved from <http://barrieaircraft.com/photo/de-havilland-canada-dhc-3-otter-02.html> on 14.07.2016.
- [8] Tidmarsh, M. and Alchin, L., Consolidated PBY Catalina, Online image, Retrieved from <http://www.airpowerworld.info/other-military-aircraft/pby-catalina-flying-boat.htm> on 14.07.2016.
- [9] Stewart, R. C., “NASA Langley Research Center, Seaplane Towing Channel”, HAER No. VA-118-C, HAER (Historic American Engineering Record Division), National Park Service, 1996.

- [10] Norton, D. A., “Airplane Drag Prediction”, Annals of the New York Academy of Sciences, Vol. 154, No. 1 (1968), pp. 306-328.
- [11] Toubin, H., “Prediction and Phenomenological Breakdown of Drag for Unsteady Flows”, Pierre et Marie Curie University, 2015.
- [12] Thomas, A. S., Saric, W. S., Braslow, A. L., Bushnell, D. M., Lock, R. C. and Hackett, J. E., “Aircraft Drag Prediction and Reduction”, Report No. 723, AGARD, 1985.
- [13] Van Dam, C. P., “Recent Experience with Different Methods of Drag Prediction”, Progress in Aerospace Sciences, Vol. 35, No. 8 (1999), pp. 751-798.
- [14] Gobbi, G., Smrcek, L., Galbraith, R., Lightening, B., Strater, B. and Majka, A., “Report on Current Strength and Weaknesses of Existing Seaplane/Amphibian Transport System As Well As Future Opportunities Including Workshop Analysis”, FUSETRA (Future Seaplane Traffic), 2011.
- [15] FAA (Federal Aviation Administration), “Integration of Civil Unmanned Aircraft Systems (UAS) in the National Airspace System (NAS) Roadmap”, Retrieved from https://nppa.org/sites/default/files/UAS_Roadmap_2013.pdf on 26.11.2016.
- [16] Unmanned Systems Technology, Singular Aircraft Flyox, Online image, Retrieved from <http://www.unmannedsystemstechnology.com/2015/07/flyox-i-amphibious-uav-completes-first-flight/singular-aircraft-flyox/> on 14.07.2016.
- [17] Mutlu, T., Coşgun, V., Kurtuluş, B., Tunca, E., Kurtuluş, D. F. and Tekinalp, O., “Su Bulanıklığı Dinamiği ve Su Parametrelerini Ölçme Kabiliyeti Olan İnsansız Hava Aracı Platformunun Geliştirilmesi [Development of Unmanned Aerial Vehicle Platform with Measurement Capabilities of Water Turbidity Dynamics and Water Parameters]”, UHAT’2012, I. Ulusal Havacılık

Teknolojisi Ve Uygulamaları Kongresi [I. National Aviation Technology and Applications Congress], İzmir, Turkey, 20-22 December, 2012.

- [18] Sivil Havacılık Genel Müdürlüğü [Directorate General of Civil Aviation], “Suya İniş Kalkış Alanları [Water Take-off and Landing Areas]”, Retrieved from <http://web.shgm.gov.tr/tr/havaalanlari/2091-suya-inis-kalkis-alanlari> on 26.11.2016.
- [19] Raymer, D. P., *Aircraft Design: A Conceptual Approach, 5th ed.*, AIAA, 2012.
- [20] Gudmundsson, S., *General Aviation Aircraft Design*, Butterworth-Heinemann, 2013.
- [21] Stinton, D., *The Design of the Aeroplane*, BSP Professional Books, 1985.
- [22] Çıray, C., *Akışkanlar Mekaniğine Giriş, Üçüncü Kitap [Introduction to Fluid Mechanics, Vol. 3]*, ODTÜ Yayıncılık, 2013.
- [23] ANSYS® Fluent, Release 15.0, Help System, Theory Guide, ANSYS, Inc., 2013.
- [24] Harris, T. A., “The 7 by 10 Foot Wind Tunnel of the National Advisory Committee for Aeronautics”, Technical Report No. 412, NACA, 1933.
- [25] Sazak, E. and Kurtuluş, D. F., “Parametric Investigation of Hull Shaped Fuselage for an Amphibious UAV”, ICCFD9 9th International Conference on Computational Fluid Dynamics, Istanbul, Turkey, 11-15 July, ICCFD9-2016-226, 2016.
- [26] Sazak, E. and Kurtuluş, D. F., “Amfibi İHA Gövde Parametrelerinin Sürüklenme Katsayısı Üzerindeki Etkilerinin İncelenmesi [Investigation of Effects of Amphibious UAV Fuselage Parameters on Drag Coefficient]”, UHUK’2016 Ulusal Havacılık ve Uzay Konferansı [National Aerospace Conference], Kocaeli, Turkey, 28-30 September, UHUK-2016-075, 2016.

- [27] Qiu, L. and Song, W., “Efficient Decoupled Hydrodynamic and Aerodynamic Analysis of Amphibious Aircraft Water Takeoff Process”, *Journal of Aircraft*, Vol. 50, No. 5 (2013), pp. 1369-1379.
- [28] Levis, E. and Serghides, V. C., “The Potential of Seaplanes as Future Large Airliners”, *Applied Aerodynamics Conference 2014: Advanced Aero Concepts, Design and Operations*, Bristol, UK, 22-24 July, 2014.

APPENDIX A

MODEL CROSS-SECTIONAL DATA

Table A.1: Offsets for NACA Model 57-A [1]

Station	Distance from F.P.	Distance from base line							Half-breadth	Deck radius	
		Keel	B1 1.20	B2 2.40	B3 3.60	B4 4.80	Chine	Deck	Chine		
F.P.	0	2.71						2.71	2.71	Tangent at 0.60	3.50
1/4	1.05	5.93	4.30	3.63				3.45	1.36	3.20	4.22
1/2	2.10	7.21	5.53	4.61	4.17			4.11	0.97	4.08	5.03
1	4.20	8.75	7.23	6.18	5.56	5.29		5.28	0.51	5.02	
1 1/2	6.30	9.66	8.40	7.39	6.70	6.33		6.26	0.24	5.53	
2	8.40	10.28	9.20	8.25	7.55	7.14		7.03	0.09	5.79	
3	12.60	10.92	10.09	9.34	8.70	8.22		8.04	0	5.97	
4	16.80	11.08	10.46	9.88	9.34	8.88		8.58	0	6.00	
5	21.00	11.09	10.60	10.13	9.67	9.22		8.84	0	6.00	
6	25.20	11.09	Straight line to chine					8.91	0	6.00	
7	29.40	11.09	Straight line to chine					8.91	0	6.00	
8	33.60	11.09	Straight line to chine					8.92	0	5.97	
9	37.80	11.09	Straight line to chine					8.96	0	5.86	
10, F	42.00	11.09	Straight line to chine					9.02	0	5.70	
10, A	42.00	10.24	Straight line to chine					8.17	0	5.70	
11	46.20	9.72	Straight line to chine					7.72	0	5.49	
12	50.40	9.21	Straight line to chine					7.30	0	5.24	

13	54.60	8.69	Straight line to chine	6.90	0	4.93	
14	58.80	8.18	Straight line to chine	6.51	0	4.57	
15	63.00	7.66	Straight line to chine	6.14	0	4.18	
16	67.20	7.14	Straight line to chine	5.77	0	3.77	
17	71.40	6.63	Straight line to chine	5.41	0	3.35	
18	75.60	6.11	Straight line to chine	5.05	0	2.92	
19	79.80	5.60	Straight line to chine	4.70	0	2.47	
A.P.	84.00	5.08	Straight line to chine	4.35	0	2.00	

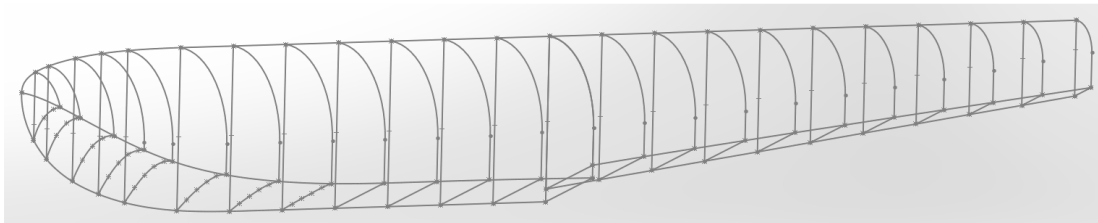


Figure A.1: View of cross-sections of NACA Model 57-A model